Nanoscale

REVIEW

View Article Online
View Journal | View Issue

Cite this: *Nanoscale*, 2021, **13**, 17989

Vacancy defect engineering of $BiVO_4$ photoanodes for photoelectrochemical water splitting

Songcan Wang, *[a] Xin Wang,[a] Boyan Liu,[a] Zhaochen Guo,[a] Kostya (Ken) Ostrikov, [b] Lianzhou Wang *[c] and Wei Huang[a]

Received 30th August 2021,
Accepted 5th October 2021

DOI: 10.1039/d1nr05691c

rsc.li/nanoscale

Photoelectrochemical (PEC) water splitting has been regarded as a promising technology for sustainable hydrogen production. The development of efficient photoelectrode materials is the key to improve the solar-to-hydrogen (STH) conversion efficiency towards practical application. Bismuth vanadate ($BiVO_4$) is one of the most promising photoanode materials with the advantages of visible light absorption, good chemical stability, nontoxic feature, and low cost. However, the PEC performance of $BiVO_4$ photoanodes is limited by the relatively short hole diffusion length and poor electron transport properties. The recent rapid development of vacancy defect engineering has significantly improved the PEC performance of $BiVO_4$. In this review article, the fundamental properties of $BiVO_4$ are presented, followed by an overview of the methods for creating different kinds of vacancy defects in $BiVO_4$ photoanodes. Then, the roles of vacancy defects in tuning the electronic structure, promoting charge separation, and increasing surface photoreaction kinetics of $BiVO_4$ photoanodes are critically discussed. Finally, the major challenges and some encouraging perspectives for future research on vacancy defect engineering of $BiVO_4$ photoanodes are presented, providing guidelines for the design of efficient $BiVO_4$ photoanodes for solar fuel production.

[a]*Frontiers Science Center for Flexible Electronics, Xi'an Institute of Flexible Electronics (IFE) and Xi'an Institute of Biomedical Materials & Engineering, Northwestern Polytechnical University, 127 West Youyi Road, Xi'an 710072, China. E-mail: iamscwang@nwpu.edu.cn*
[b]*School of Chemistry and Physics and Centre for Materials Science Queensland University of Technology Brisbane, QLD 4000, Australia*
[c]*Nanomaterials Centre, Australian Institute for Bioengineering and Nanotechnology and School of Chemical Engineering, The University of Queensland, Brisbane, Queensland 4072, Australia. E-mail: l.wang@uq.edu.au*

1. Introduction

The growth of global population and the development of industry have boosted the demand for energy. However, the contemporary society is heavily dependent on fossil fuels such as petroleum, coal and natural gas. The accelerating consumption of fossil fuels not only causes the depletion of non-renew-

Songcan Wang

Songcan Wang is currently a professor at the Institute of Flexible Electronics (IFE), Northwestern Polytechnical University (NPU), China. He received his B.Eng. (2011) and M.Eng. (2014) from Central South University (CSU), China, and PhD degree from the University of Queensland (UQ), Australia in 2018. Before joining NPU, he worked as a postdoctoral research fellow in Professor Lianzhou Wang's group at UQ for about 1.5 years. His research interests focus on the synthesis of semiconductor nanomaterials for solar energy conversion and storage, including photoelectrochemical cells, photocatalysis, and rechargeable batteries.

Kostya (Ken) Ostrikov

Kostya (Ken) Ostrikov is a Professor with Queensland University of Technology, Australia, a Founding Leader of the CSIRO–QUT Joint Sustainable Processes and Devices Laboratory, and Academician of the Academy of Europe and the European Academy of Sciences. His research focuses on nanoscale control of energy and matter contributing to the solution of the grand challenge of directing energy and matter at nanoscales, to develop renewable energy and energy-efficient technologies for a sustainable future.

able energy, but also increases the emission of CO_2 into the atmosphere.[1–5] Consequently, our human community needs to confront the severe threat of the energy crisis and environmental issues. Therefore, sustainable development has become the consensus among all nations and regions throughout the world. The development of cutting-edge technologies for the production of clean and renewable energy is the pursuit for scientists. Solar energy is the most abundant renewable energy source on earth. The solar energy reaching the earth in one hour is almost equal to the global energy demand in one year.[6] Nevertheless, the low energy density and intermittence make the direct utilization of solar energy unfavourable. Therefore, it is desirable to develop suitable technologies for efficient utilization of solar energy. Photoelectrochemical (PEC) water splitting that converts solar energy into hydrogen as the carbon-free energy carrier has been regarded as a promising technology for solar energy utilization.[7–10] PEC water splitting can store solar energy in the chemical bonds of hydrogen, and hydrogen can be used whenever required. An ideal PEC water splitting system for practical applications should be fulfilled with a high solar-to-hydrogen (STH) conversion efficiency (>10%), long-term stability, and low cost.[11] However, practical application of PEC water splitting has not been realized in the past five decades due to the very low STH efficiency achieved in the cost-effective systems.[12–14]

The STH efficiency is mainly determined by the photoelectrode materials since the three main PEC processes take place at the photoelectrode materials: (1) light absorption to generate electron–hole pairs; (2) charge separation and transport; (3) transfer of photogenerated charge carriers from the photoelectrode material to the electrolyte for surface reactions.[15–17] Amongst the above-mentioned processes, light absorption is determined by the bandgap of a semiconductor, which determines the theoretical maximum of STH efficiency under AM 1.5 G illumination. Charge separation and transport are determined by the electronic properties of the photoelectrode materials, whereas surface charge transfer properties are mainly determined by the surface catalytic activity of the photoelectrode materials. Therefore, the development of efficient photoelectrode materials is the most important task to achieve high-performance PEC water splitting. In the past five decades, numerous photoelectrode materials including oxides (*e.g.* TiO_2, WO_3, $BiVO_4$, Cu_2O, Fe_2O_3),[18–24] nitrides (*e.g.* TaON, Ta_3N_5, C_3N_4),[25–31] chalcogenides (*e.g.* MoS_2, $CuInS_2$, CZTS, CIGS),[32–37] and metal halide perovskites (*e.g.* *p*-$MAPbI_3$)[38–41] have been developed as photoelectrode materials since the first discovery of PEC water splitting in 1972.[42] However, ideal photoelectrode materials to drive PEC water splitting towards practical applications are still lacking.

Amongst all the available photoelectrode materials, bismuth vanadate ($BiVO_4$) has emerged as one of the most promising photoanode materials for PEC water splitting due to its narrow bandgap for visible light absorption, appropriate band edge positions that require a relatively low onset potential, low cost, and high stability in aqueous solutions, and has been intensively studied.[43–47] In the past decades, monoclinic scheelite-phase $BiVO_4$ has been confirmed to be an excellent photoanode material for water oxidation.[48] Although the photocatalytic water oxidation performance of $BiVO_4$ has been studied since 1998,[49] the PEC performance of $BiVO_4$ photoanodes was moderate due to the lack of suitable methods for the fabrication of efficient $BiVO_4$ films. Since 2003, with the successful synthesis of $BiVO_4$ films by metal–organic decomposition (MOD),[50] the performance of $BiVO_4$ was boosted and an increasing number of efficient methods have been developed.[51–54] Pure $BiVO_4$ photoanodes suffer from severe charge recombination because of the relatively low carrier mobility and short hole diffusion length, leading to very poor PEC performance.[55] To improve the PEC perform-

Lianzhou Wang

Lianzhou Wang is currently a professor in the School of Chemical Engineering and the director of the Nanomaterials Centre at the University of Queensland, Australia. After receiving his PhD degree from the Shanghai Institute of Ceramics in 1999, he worked at NIM and AIST in Japan for 5 years. Since 2004, he has been working at the University of Queensland and his research interest focuses on the design and development of semiconducting materials toward efficient solar energy conversion and storage.

Wei Huang

Wei Huang received his B.Sc., M.Sc., and Ph.D. in chemistry from Peking University in 1983, 1988, and 1992, respectively. He was appointed as the Deputy President of Nanjing University of Posts and Telecommunications in 2006, the President of Nanjing Tech University in 2012, and the Provost of Northwestern Polytechnical University in 2017. He is a member of the Chinese Academy of Sciences, Foreign Academician and Honorary Doctor of the Russian Academy of Sciences, and Fellow of the Royal Society of Chemistry. His research interests include organic optoelectronics, nanomaterials, polymer chemistry, plastic electronics, and bioelectronics.

ance of $BiVO_4$ photoanodes, various strategies such as heterojunction formation,[56–61] heteroatom doping,[62–65] nanostructure construction,[66–68] photo-charging,[69–74] crystal facet engineering,[75–78] and vacancy defect engineering[79–82] have been developed, which can effectively enhance light absorption, charge separation and transport, or surface charge transfer properties.

Owing to the rapid progress of $BiVO_4$ photoanodes, several review articles discussing nanostructure engineering,[83] crystal facet engineering,[84] and modification strategies[85] to improve the PEC performance of $BiVO_4$ have been reviewed. In recent years, vacancy defect engineering has emerged as an important and efficient strategy to tailor the optoelectronic structure of photoelectrode materials.[86–92] In particular, an increasing number of studies on vacancy defect engineering of $BiVO_4$ photoanodes including the generation of oxygen vacancies, vanadium vacancies, and bismuth vacancies have been reported.[93–99] Since vacancy defects serve as self-dopants in tailoring the conductivity, band edge positions and surface molecular adsorption properties of $BiVO_4$ photoanodes, the PEC performance can be effectively improved.[100] Considering the rapid development and increasing interest in this important field, a comprehensive and timely review solely focusing on analysing the formation of vacancy defects in $BiVO_4$ photoanodes and their roles in promoting the PEC performance is urgently needed. In this review article, some general properties of $BiVO_4$ such as crystal structures, optical properties, carrier transport, and photogenerated carrier lifetime are briefly introduced. This is followed by an overview of the formation of oxygen vacancies, vanadium vacancies, and bismuth vacancies in $BiVO_4$ photoanodes. Subsequently, the roles of vacancy defects in $BiVO_4$ photoanodes are critically discussed. Finally, a concise summary of vacancy defect engineering of $BiVO_4$ photoanodes for PEC water splitting, the key challenges and perspectives in this attractive field are presented. We hope to shed light on the development of vacancy defect engineering for the design of efficient photoelectrodes for solar fuel production.

2. Crystal structure and optical and electronic properties

$BiVO_4$ is a bright yellow solid that is generally applied as a novel environmentally friendly inorganic yellow pigment because of its high hiding power, weather resistance, and non-toxic feature.[101,102] The bandgap of $BiVO_4$ is 2.4–2.5 eV, which can absorb visible light up to approximately 520 nm. In addition, the valence band maximum (VBM) of $BiVO_4$ is more positive than the water oxidation potential, making $BiVO_4$ an attractive photoanode material for PEC water splitting. Since crystal, optical and electronic structures have a close relationship with the PEC performance of $BiVO_4$ photoanodes, in this section, we will briefly introduce the crystal, optical and electronic properties of $BiVO_4$ and critically discuss their effects on PEC water splitting performance, which is essential for the design of efficient $BiVO_4$ photoanodes.

2.1. Crystal structures

As shown in Fig. 1, $BiVO_4$ has three main crystal forms: *pucherite*, *dreyerite* and *clinobisvanite*.[48,83] More specifically, *pucherite* is a natural mineral of $BiVO_4$ with an orthorhombic crystal structure, which cannot be synthesized by general laboratory routes. *Dreyerite* occurs in a tetragonal zircon (t-z) structure, whereas *clinobisvanite* is a monoclinic scheelite (m-s) structure. In addition, when the atomic positions are modified to construct a four-fold symmetry structure in the *clinobisvanite*, another tetragonal scheelite (t-s) structure is formed. The crystal structures and bond lengths of $BiVO_4$ are listed in Table 1.[103] Both *dreyerite* and *clinobisvanite* can be prepared in the laboratory under different conditions. Generally, $BiVO_4$ (m-s) is achieved by a solid-state reaction at high temperatures.[104] In addition, sol–gel and hydrothermal methods can also obtain $BiVO_4$ (m-s).[105] $BiVO_4$ (t-z) is synthesized in aqueous media by low-temperature processes. For example, $BiVO_4$ (t-z) was prepared *via* a coprecipitation method using a $Bi(NO_3)_3$ solution containing nitric acid and an aqueous NH_4VO_3 solution at room temperature.[106]

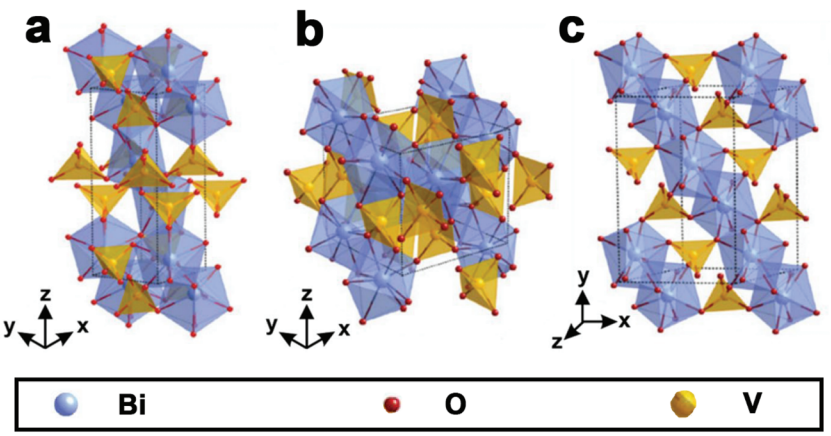

Fig. 1 Crystal structure of $BiVO_4$: (a) *pucherite*, (b) *dreyerite* and (c) *clinobisvanite*. Reproduced from ref. 107 with permission. Copyright 2016, Springer Nature.

Table 1 Crystal structures of $BiVO_4$ with different space groups and bond lengths[103]

Crystal System	Orthorhombic	t-z	m-s	t-s
Crystal structure (Å)				
Space group	*Pnca*	$14_1/amd$	C_2/c	$14_1/a$
A	5.332	7.303	7.247	5.147
B	5.060	7.303	11.697	5.147
C	12.020	6.584	5.090	11.722
Bond length (Å)				
Bi–O	2.20	2.41	2.35	2.40
	2.31	2.55	2.37	2.47
	2.53		2.52	
	2.73		2.63	
V–O	1.76	1.7	1.69	1.73
	2.73		1.76	

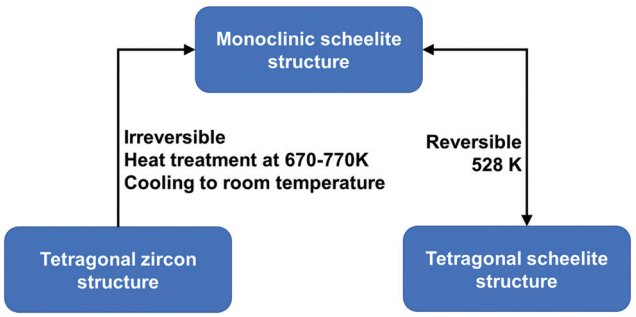

Fig. 2 Conditions for phase transformation between different crystal structures of $BiVO_4$. Reproduced from ref. 108 with permission. Copyright 2001, American Chemical Society.

$BiVO_4$ (m-s) can be transformed from both $BiVO_4$ (t-z) and $BiVO_4$ (t-s) by a thermal treatment process. As illustrated in Fig. 2, by annealing $BiVO_4$ (t-z) at 670–770 K, followed by cooling to room temperature, $BiVO_4$ (m-s) can be obtained. However, $BiVO_4$ (m-s) cannot be converted back to $BiVO_4$ (t-z) by thermal treatment. $BiVO_4$ (t-s) is a high temperature phase and the phase transition between $BiVO_4$ (t-s) and $BiVO_4$ (m-s) is reversible at 528 K.[108] Interestingly, different crystalline structures of $BiVO_4$ nanoparticles (t-z, m-s, and t-z/m-s heterostructure) can be synthesized by a fast microwave assisted method and annealing treatment process.[109]

The photocatalytic activity of $BiVO_4$ is affected by its crystal structure. For example, $BiVO_4$ powders with m-s and t-z structures were selectively prepared by tuning the ratio of vanadium to bismuth in the starting materials.[110] The bandgap of $BiVO_4$ (t-z) is 2.9 eV while that of $BiVO_4$ (m-s) is 2.4 eV, as demonstrated in Fig. 3a. As a result, $BiVO_4$ (t-z) and $BiVO_4$ (m-s) showed similar photocatalytic activities under UV light ($300 < \lambda < 380$ nm) illumination in the presence of silver nitrate as the electron sacrificial reagent. However, $BiVO_4$ (m-s) exhibited a much higher photocatalytic activity than $BiVO_4$ (t-z) under visible light ($\lambda > 420$ nm) illumination. Therefore, the different photocatalytic activity between $BiVO_4$ (t-z) and $BiVO_4$ (m-s) is mainly derived from their different bandgaps. $BiVO_4$ powder with a scheelite structure was prepared by hydrolysing a mixture of $Bi(NO_3)_3$ and Na_3VO_4 solution containing nitric acid with Na_2CO_3 or $NaHCO_3$ at room temperature.[108] By tuning the reaction time, $BiVO_4$ (t-s) and $BiVO_4$ (m-s) can be selectively obtained. This pioneering work provides a reliable process for the synthesis of the high-temperature formed $BiVO_4$ (t-s) at room temperature, enabling the possible study of

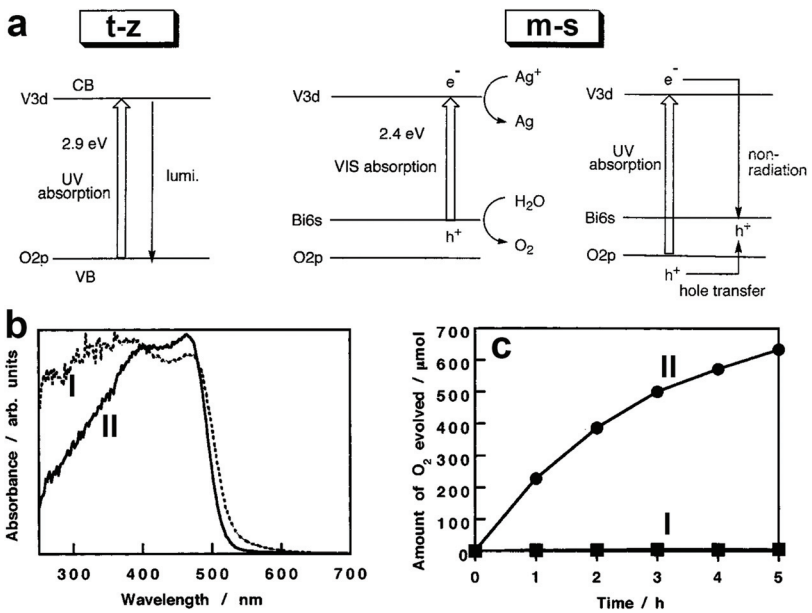

Fig. 3 (a) Band structures of the t-z and m-s $BiVO_4$. Reproduced from ref. 110 with permission. Copyright 1999, American Chemical Society. (b) UV-vis light absorption curves and (c) oxygen evolution curves in an aqueous $AgNO_3$ solution under visible light illumination ($\lambda > 420$ nm) of the $BiVO_4$ samples I: $BiVO_4$ (t-s) and II: $BiVO_4$ (m-s). Reproduced from ref. 108 with permission. Copyright 2001, American Chemical Society.

its photocatalytic activity. Interestingly, even though $BiVO_4$ (t-s) and $BiVO_4$ (m-s) exhibit very similar crystal structures and bandgaps (Fig. 3b), their photocatalytic activities are significantly different. $BiVO_4$ (m-s) showed a high photocatalytic activity for O_2 evolution in an aqueous $AgNO_3$ solution under visible light illumination, whereas its $BiVO_4$ (t-s) counterpart exhibited a negligible O_2 evolution activity (Fig. 3c). It was believed that the high visible light photocatalytic activity of $BiVO_4$ (m-s) is attributed to the distortion of a Bi–O polyhedron by a $6s^2$ lone pair of Bi^{3+} that induces the local polarization, promoting the separation of photogenerated electron–hole pairs.

2.2. Optical properties

According to the discussion in section 2.1, $BiVO_4$ (m-s) exhibits the best photocatalytic activity, and has been widely studied as an excellent water oxidation material for both photocatalytic and PEC water splitting.[111–115] Therefore, the optical properties discussed in this section are focused on $BiVO_4$ (m-s). Based on the density functional theory (DFT) calculations, the minimum bandgap of $BiVO_4$ is 2.174 eV, and the two *k*-points at the VBM and conduction band minimum (CBM) are located at different positions, indicating the indirect bandgap characteristics (Fig. 4a).[116] The calculated bandgap is underestimated compared to the experimental values (2.4–2.5 eV depending on the preparation methods), due to the well-known drawback of generalized gradient approximation (GGA). The band structure of $BiVO_4$ is shown in Fig. 4b, where the conduction band of $BiVO_4$ mainly originates from the V 3d orbitals, while the valence band is composed of the hybridization of the O 2p and Bi 6s orbitals,[117] which is consistent with the band structure proposed by Kudo *et al.*[110] Owing to the relatively narrow bandgap and the positive VBM, $BiVO_4$ exhibits excellent photocatalytic oxygen evolution and organic compound decomposition under visible light illumination.[118–120] However, since the CBM of $BiVO_4$ is close to but a little more positive than the hydrogen evolution potential, spontaneous photocatalytic hydrogen evolution cannot take place. Thus, $BiVO_4$ can only achieve the half water oxidation reaction. As shown in Fig. 4c, the absorption coefficient (α) of pure $BiVO_4$ increases significantly at the bandgap energy, with a value of 1×10^4 cm^{-1} at the band edge absorption onset of approximately 500 nm, reaching 1×10^5 cm^{-1} at around 460 nm.[121] Moreover, a plateau can be observed between 430 and 390 nm. When the wavelength is shorter than 390 nm, the absorption coefficient increases gradually. The strong absorption of green to ultraviolet photons in the visible region and transmission of yellow to infrared photons results in the yellow colour of $BiVO_4$.

2.3. Carrier transport

The efficient transport of majority charge carriers in $BiVO_4$ is essential to achieve a high charge separation efficiency when used as a photoanode. Previous experimental studies revealed that the carrier transport in $BiVO_4$ photoanodes is poor, leading to severe charge recombination. However, the underlying mechanism was unclear due to the lack of cutting-edge time-resolved technology to characterize the dynamic charge separation and transport process. In 2013, Roel van de Krol's group applied a time-resolved microwave conductivity (TRMC) technology to investigate $BiVO_4$ under one sun illumination, and found that the carrier mobility of undoped $BiVO_4$ is ~0.04 cm^2 V^{-1} s^{-1}, which is at least 1–2 orders of magnitude lower than that of other typical semiconductor photoelectrode materials (*e.g.* the electron mobility of ZnO is 100–200 cm^2 V^{-1} s^{-1}) for PEC water splitting.[122] DFT calculations revealed that the low carrier mobility is attributed to the relatively localized charge carriers due to the weakly dispersive valence band and conduction band in the band structure curve. By using THz

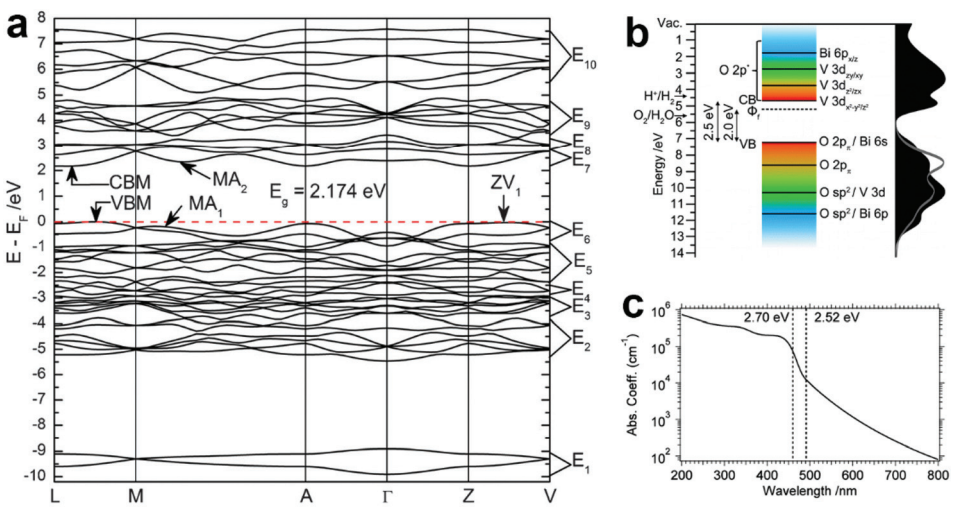

Fig. 4 (a) The calculated band structure of $BiVO_4$ (m-s). Reproduced from ref. 116 with permission. Copyright 2011, Royal Society of Chemistry. (b) Schematic illustration of the band structure of $BiVO_4$ (m-s). Reproduced from ref. 117 with permission. Copyright 2014, American Chemical Society. (c) The absorption coefficient curve of $BiVO_4$ (m-s) between 200 and 800 nm. Reproduced from ref. 121 with permission. Copyright 2015, American Chemical Society.

spectroscopy, the temporal evolution of polaron formation leading to a build-up of a polaron population in parallel to initial carrier trapping was observed in $BiVO_4$.[123] In addition, the self-trapped carriers have a mobility of 0.02 $cm^2\ V^{-1}\ s^{-1}$, leading to a thermal hopping activation energy of ~90 meV. Interestingly, $BiVO_4$ showed facet-dependent charge carrier transport properties.[124] The effective hole and electron masses of the (010) facet are estimated to be approximately $0.16m_0$ and $0.11m_0$, respectively. In comparison, the effective hole and electron masses of the (011) facet are around $0.40m_0$ and $0.24m_0$, respectively. Since the drift velocity of electrons or holes is proportional to the reciprocal of the effective mass, lower effective masses indicate more efficient charge carrier transport. Therefore, charge carrier transport properties in the (010) facet are better than those in the (011) facet for $BiVO_4$. In addition, O 2p and Bi 6s contributions in the valence bands are more localized in the (011) facet compared to those of the (010) facet. Thus, the (011) facet exhibits slower charge mobility than the (010) facet.

On the other hand, the relatively low electronic conductivity also causes severe charge recombination in $BiVO_4$ photoanodes. Doping $BiVO_4$ with either Mo^{6+} or W^{6+} or simultaneous doping with Mo^{6+} and W^{6+} at the V^{5+} site is effective to increase the electronic conductivity,[125–128] thereby promoting the PEC water splitting performance. Generally, the increased carrier density after doping can be demonstrated from Mott–Schottky plots. Interestingly, DFT calculations revealed a marginal decrease in the value of carrier mobility with an increase in the doping level (singly and co-doped samples), which is consistent with the experimental results that the intrinsic mobility of electrons in doped $BiVO_4$ is smaller than that in un-doped $BiVO_4$.[129] However, W/Mo doping is efficient to increase the electron carrier concentration, leading to higher conductivity of the $BiVO_4$ photoanode.

2.4. Photogenerated carrier lifetime

In addition to the excellent conductivity for majority charge carriers, a promising photoanode should also efficiently transport photogenerated minority charge carriers to the semiconductor/electrolyte interfaces for water oxidation. Therefore, the lifetime of the photogenerated carriers is another important factor. The minority carrier diffusion length (L) is defined by $L = (D\tau)^{1/2}$,[130] where D is the diffusion constant, which is proportional to the carrier mobility, and τ is the minority carrier lifetime, which is highly sensitive to the crystal structure, crystallinity, facet and recombination channels in the semiconductor. According to this equation, a higher carrier mobility and a longer minority carrier lifetime can achieve a longer minority carrier diffusion length, which means that the photogenerated charge carriers are easier to be separated and transferred to the semiconductor/electrolyte interface for the subsequent photocatalytic reaction.

Since $BiVO_4$ has an indirect bandgap, the band edge photoluminescence curve cannot be observed and the direct measurement of the minority carrier lifetime through time-resolved photoluminescence cannot be achieved. Thus, transient absorption pump–probe spectroscopy was applied to determine the characteristic relaxation time.[121] By using excitation pulses at 350 nm with a duration of 100 fs and a repetition rate of 1 kHz, and a white light continuum pulse of 360–700 nm, the decay time was estimated to be around 20 ns. In another study, TRMC measurements confirmed that the carrier lifetime of $BiVO_4$ is exponentially long, reaching ~40 ns.[122] Although the carrier lifetime of $BiVO_4$ is much longer than that of other metal oxide semiconductors such as α-Fe_2O_3 (3 ps), WO_3 (1–9 ns), and Cu_2O (40 ps), the minority carrier diffusion length of $BiVO_4$ is calculated to be only ~70 nm, due to the relatively low carrier mobility. It was believed that the relatively long carrier lifetime is attributed to the indirect bandgap characteristics of $BiVO_4$ that prevent a direct recombination of the photogenerated hole–electron pairs.[131]

Interestingly, $BiVO_4$ particles exhibit particle size dependent carrier dynamics and reactivity under visible light illumination, as evidenced by single-particle transient absorption microscopy.[132] Upon the illumination of a 527 nm light, it was found that the well-faceted nano-aggregated $BiVO_4$ crystals exhibit fast hole decay and little reactivity for Fe^{3+} reduction. In comparison, other aggregated particles with grain boundaries between small primary crystals exhibit slower hole decay and higher reactivity for Fe^{3+} reduction than their nano-aggregated crystal counterparts. When the secondary particle size of the aggregated crystals increases, the hole decay becomes slower and the reactivity becomes higher. Thus, the grain boundaries in aggregated particles do not function as recombination centers but play an essential role in elongating the carrier lifetime.

3. Vacancy defect engineering of $BiVO_4$ photoanodes

In the conventional point of view, vacancy defects in semiconductor materials would induce detrimental effects on their photocatalytic activities. In fact, excessive vacancy defects in semiconductor materials lead to enhanced charge recombination due to the generation of more charge recombination centers.[133,134] Nevertheless, an optimized number of vacancy defects can effectively tailor the electronic structure of a semiconductor material, and increase the conductivity and mobility, thereby promoting photocatalytic activity. In recent years, an increasing number of publications confirmed the benefit of vacancy defects in photoelectrode materials for PEC water splitting.[135–140] In particular, oxygen vacancies function as shallow donors in $BiVO_4$ photoanode materials, which can improve the electronic conductivity and promote the separation and transfer of photogenerated charge carriers.[141] As a result, a much higher photocurrent density can be observed compared to pristine $BiVO_4$ photoanodes without vacancy defects.

In addition to tuning the electronic structure, oxygen vacancies can also cause distortions in the crystal structure of

$BiVO_4$ at room temperature, and the degree of distortion is determined by the vacancy concentration.[142] Moreover, defects on the surface of $BiVO_4$ can obviously increase the hydrophilicity, promoting the surface water oxidation reaction.[143] Generally, most of the oxide semiconductors show n-type conductivity due to the formation of oxygen vacancies, whereas the formation of cationic vacancies or interstitial anions could increase the p-type conductivity.[144,145] This is very interesting, because the switchable n–p conductivity of a metal oxide semiconductor can be designed by deliberately creating oxygen vacancies or cationic vacancies. With the increasing interest of vacancy defect engineering in PEC water splitting, other kinds of vacancy defects such as vanadium vacancies and bismuth vacancies have also been prepared. In this section, we will concisely discuss the methods to generate different kinds of vacancy defects in $BiVO_4$ photoanodes, and critically analyse the roles of vacancy defects in $BiVO_4$ photoanodes in terms of improving the PEC properties.

3.1. Formation of vacancy defects in $BiVO_4$ photoanodes

3.1.1. Oxygen vacancies. Oxygen vacancies can increase the carrier densities in $BiVO_4$ photoanodes, which increases band bending at the semiconductor/electrolyte interfaces, thus promoting charge separation and transfer.[141] As shown in Fig. 5, strategies such as thermal treatment under a reduction/inert atmosphere, chemical reduction, electrochemical reduction, photo/PEC treatment, precursor solution/film treatment, and heteroatom doping have been developed for generating oxygen vacancies in $BiVO_4$ photoanodes. In this subsection, we will briefly introduce the above emerging strategies for the generation of oxygen vacancies in $BiVO_4$ photoanodes.

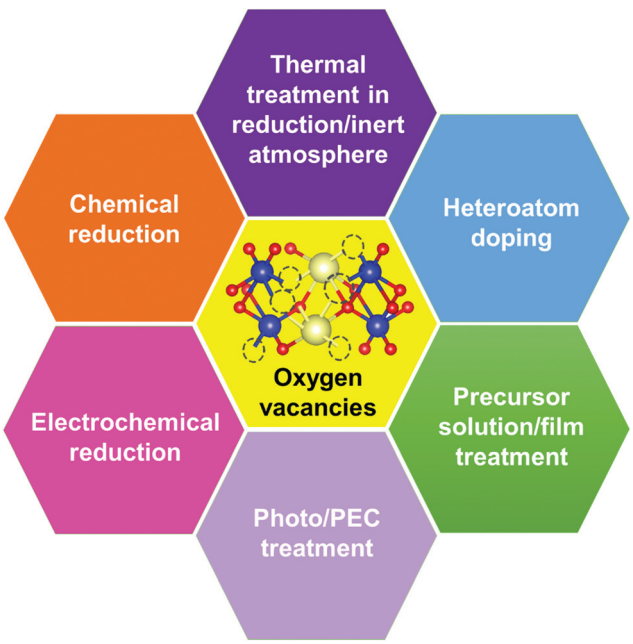

Fig. 5 Strategies for generating oxygen vacancies in $BiVO_4$ photoanodes.

Generally, thermally treating a metal oxide semiconductor under a reduction or inert atmosphere can generate oxygen vacancies. The number of generated oxygen vacancies can be tailored by controlling the thermal treatment temperature. The formation of oxygen vacancies can be expressed using the Kröger–Vink notation:[146]

$$O_O^{\times} \rightarrow V_O^{\cdot\cdot} + \frac{1}{2}O_2 + 2e' \quad (1)$$

$$e' + V_V^{\times} \rightarrow V_V^{'} \quad (2)$$

$$e' + Bi_{Bi}^{\times} \rightarrow Bi_{Bi}^{'} \quad (3)$$

According to eqn (1)–(3), the formation of one oxygen vacancy ($V_O^{\cdot\cdot}$) is accompanied by the reduction of one V^{5+} ($V_V^{\times}$) and one Bi^{3+} ($Bi_{Bi}^{\times}$) to generate V^{4+} ($V_V^{'}$) and Bi^{2+} ($Bi_{Bi}^{'}$), thus maintaining electric neutrality in the $BiVO_4$ crystal.

Planar $BiVO_4$ films were annealed under a hydrogen atmosphere at elevated temperatures between 200 and 400 °C.[147] Not only oxygen vacancies but also hydrogen impurities were incorporated into the $BiVO_4$ films. With the annealing temperature increased from 200 to 400 °C, the bright yellow $BiVO_4$ films turned yellowish green and eventually dark green. Similarly, nanoporous $BiVO_4$ films were prepared by a typical electrodeposition-thermal method.[66] To create oxygen vacancies, the obtained nanoporous $BiVO_4$ films were annealed in a flow of 6% H_2/Ar for 10 min at 300 °C.[82] In addition to hydrogen treatment at elevated temperatures, hydrogen plasma treatment of $BiVO_4$ photoanodes at room temperature can also generate oxygen vacancies.[148] Likewise, the number of oxygen vacancies in three-dimensional (3D) nanoporous $BiVO_4$ can be controllably generated by an ionized argon plasma technology.[149] Moreover, anoxic annealing can also generate oxygen vacancies in $BiVO_4$ photoanodes, which was effective to increase the mobility, lifetime, and concentration of the photogenerated carriers.[150] In addition, thermally treating $BiVO_4$ under an argon atmosphere at elevated temperature can also generate oxygen vacancies.[151] Unlike under the hydrogen atmosphere, a higher temperature (*e.g.* 500 and 700 °C) is required to generate oxygen vacancies under an argon atmosphere, which can form new sub-gap states in the electronic structure of $BiVO_4$.

Chemical reduction of $BiVO_4$ photoanodes with different reducing agents is another common strategy to generate oxygen vacancies. By chemically treating $BiVO_4$ films in a $NaBH_4$ solution, B–O bonding at the surface of $BiVO_4$ photoanodes was destroyed, leading to the removal of oxygen atoms and the formation of oxygen vacancies.[152] In addition, Bi^{3+} ions were reduced to metallic Bi nanoparticles that were decorated homogeneously on the surfaces of the $BiVO_4$ photoanode. Similarly, an effective surface-engineered sulfite treatment process was developed to generate surface oxygen vacancies in $BiVO_4$ photoanodes without illumination.[153] Interestingly, a novel pyramid-$BiVO_4$ with sufficient oxygen vacancies was prepared by a low-temperature solvothermal

process,[154] which can effectively improve the separation and transfer efficiencies of the photogenerated charge carriers.

Electrochemical reduction can also generate oxygen vacancies in $BiVO_4$ photoanodes. The number of oxygen vacancies generated can be tuned by controlling the reduction potential and the electrochemical reduction time. For example, an electrochemical reduction process was applied to treat the Mo-doped $BiVO_4$ films.[155] As shown in Fig. 6a, when the $BiVO_4$ film was electrochemically treated at −0.8 V (*versus* Ag/AgCl), a quasi-oxygen vacancy was formed on the (020) facet (only Bi–O bonds crack), which can significantly increase the electron mobility and photocurrent density. Nevertheless, the reduction potential of −1.2 V induced the formation of oxygen vacancies on the surface of the (020) facet (both Bi–O and V–O bonds break simultaneously), leading to the obvious decrease of photocurrent densities. It was believed that the formation of a quasi-oxygen vacancy is essential to promote the PEC water splitting performance of the Mo-doped $BiVO_4$ photoanodes, as evidenced by the much weaker photoluminescence signal of the −0.8-BiMoVO compared to that of BiMoVO (Fig. 6b). Similarly, a hydrothermally synthesized $BiVO_4$ film with the (040) facet grown vertically on the fluorine doped SnO_2 (FTO) glass substrate (Fig. 6c–e) was electrochemically treated at −0.1 V *versus* the reversible hydrogen electrode (RHE) for only 150 s, which generated an appropriate amount of oxygen vacancies.[79] Surprisingly, the photocurrent density is significantly enhanced by 10 times, reaching 2.5 mA cm^{-2} under AM 1.5 G illumination (Fig. 6f). Upon the surface modification with cobalt borate (CoBi) as the oxygen evolution co-catalyst, the photocurrent density can be further improved, exhibiting an excellent applied bias photon-to-current efficiency (ABPE) of 1.1%.

Interestingly, photo or PEC treatment of $BiVO_4$ photoanodes in the presence of Na_2SO_3 solution can also generate oxygen vacancies. The formation of oxygen vacancies is attributed to the redox reaction capacity of the photogenerated electrons and holes, as demonstrated below:[95,156]

$$e' + V_V^{\times} \rightarrow V_V^{'} \quad (4)$$

$$e' + Bi_{Bi}^{\times} \rightarrow Bi_{Bi}^{'} \quad (5)$$

$$2h^{\bullet} + O_O^{\times} + SO_3^{2-}(\text{in solution}) \rightarrow SO_4^{2-}(\text{in solution}) + V_O^{\bullet\bullet} \quad (6)$$

For example, a bare $BiVO_4$ photoanode was placed in a Na_2SO_3 solution under light illumination.[156] Owing to the presence of a hole sacrificial agent (Na_2SO_3), the photogenerated holes are consumed while the photogenerated electrons can reduce $BiVO_4$ itself, forming oxygen vacancies. Similarly, a facile photoetching process was applied to generate enriched oxygen vacancies at the surface of $BiVO_4$ photoanodes, while avoiding the formation of excessive bulk defects.[95] The surface oxygen vacancies increased the carrier density to enhance

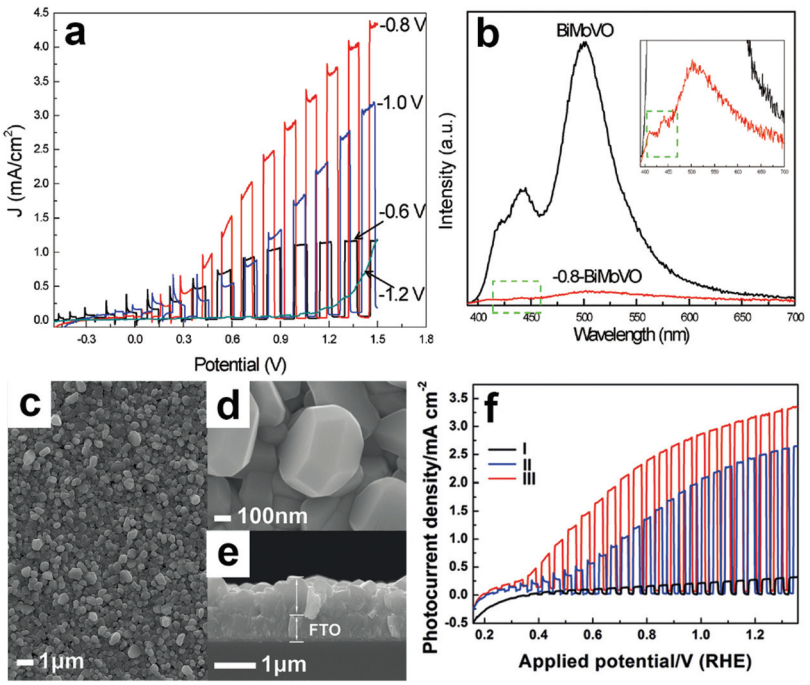

Fig. 6 (a) Photocurrent density *versus* applied potential curves of the Mo-doped $BiVO_4$ films electrochemically treated at −0.6, −0.8, −1.0, and −1.2 V *versus* Ag/AgCl, respectively. (b) Photoluminescence spectra of Mo-doped $BiVO_4$ without electrochemical reduction (BiMoVO) and electrochemically treated at −0.8 V (−0.8-BiMoVO). Reproduction from ref. 155 with permission. Copyright 2017, Wiley-VCH. (c) Low-magnification, (d) high-magnification, and (e) cross-sectional SEM images of $BiVO_4$ films with (040) facet grown vertically on the FTO substrate. (f) Photocurrent density *versus* applied potential curves of samples I: BVO_4 film, II: electrochemically-treated $BiVO_4$ film (E-BVO), and III: CoBi/E-BVO. Reproduced from ref. 79 with permission. Copyright 2017, Wiley-VCH.

band bending, leading to a 2.3-fold higher charge separation efficiency. Recently, a PEC activation process was developed to generate oxygen vacancies at the surface and passivated the surface states for $BiVO_4$ photoanodes, thus boosting charge transfer at the $BiVO_4$/electrolyte interface, suppressing surface recombination, and leading to an enhanced PEC performance.[94]

Suitable treatment on the precursor solutions or films can also generate oxygen vacancies in the obtained $BiVO_4$ photoanodes. For example, $BiVO_4$ photoanodes were prepared by a spray pyrolysis process.[157] By treating the precursor solution with ultraviolet light and ultrasonication (Fig. 7a), the nanostructure as well as the number of oxygen vacancies can be tuned in the final obtained $BiVO_4$ films. Systematic studies revealed that the nanoporous structure was mainly attributed to the ultrasonic treatment, while the formation of oxygen vacancies was primarily derived from ultraviolet treatment. Bismuth precursor films were prepared by an electrodeposition method.[158] By thermally treating the bismuth precursor films with vanadyl acetylacetonate ($VO(C_5H_7O_2)_2$) vapors (Fig. 7b), $BiVO_4$ films with abundant oxygen vacancies can be achieved. Interestingly, the number of oxygen vacancies in the $BiVO_4$ film can be tuned by changing the pH value in the precursor electrolyte. $BiVO_4$ films obtained by converting from the bismuth precursor films electrodeposited in an acidic electrolyte contain much more oxygen vacancies compared to their counterparts prepared by electrodeposition in an alkaline electrolyte (Fig. 7c). A bismuth oxide precursor film was prepared by an electrodeposition method, which was converted to a transparent $BiVO_4$ photoanode with well-controlled oxygen vacancies through a mild thermal treatment process in the presence of $VO(C_5H_7O_2)_2$.[80] The formation of a bismuth oxide precursor film is the key to generate oxygen vacancies in the obtained $BiVO_4$ photoanode. By carefully tuning the electrodeposition and the thermal treatment processes, an appropriate amount of oxygen vacancies was formed in the $BiVO_4$ photoanodes, leading to a significantly enhanced charge separation efficiency. As a result, a high photocurrent density of 5.87 mA cm^{-2} was achieved at 1.23 V *versus* RHE under AM 1.5 G illumination (Fig. 7d and e). Very recently, a new sulfur oxidation strategy was developed to prepare planar $BiVO_4$ photoanodes with *in situ* formed oxygen vacancies.[81] The oxidation of sulfur during the calcination process can create an oxygen deficient atmosphere, leading to the formation of oxygen vacancies in the $BiVO_4$ photoanodes.

Doping $BiVO_4$ photoanodes with other elements can induce the formation of oxygen vacancies. Both theoretical and experimental results revealed that Zn doping can replace the Bi-sites, thus inducing a controllable number of oxygen vacancies in the $BiVO_4$ films (Fig. 7f).[159] Electron paramagnetic resonance

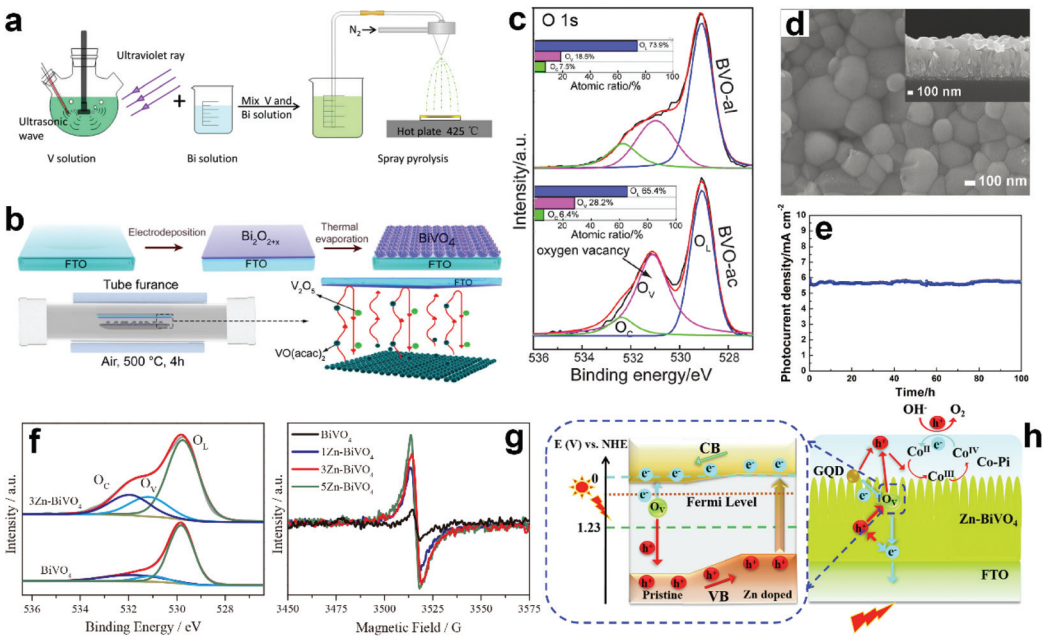

Fig. 7 (a) Schematic illustration of the preparation of nanoporous $BiVO_4$ photoanodes with abundant oxygen vacancies. Reproduced from ref. 157 with permission. Copyright 2020 Author(s). (b) Schematic illustration of the $BiVO_4$ films prepared by a thermal evaporation process. (c) High resolution XPS O 1s spectra of $BiVO_4$ films converted from bismuth precursor films prepared in an acidic electrolyte (BVO-ac) and alkaline electrolyte (BVO-al) (Inset: atomic ratios of O_L, O_V, and O_C calculated from the XPS spectrum of O 1s). Reproduced from ref. 158 with permission. Copyright 2019, Wiley-VCH. (d) SEM image of the $BiVO_4$ film with oxygen vacancies, inset: the corresponding cross-sectional view. (e) Photocurrent density *versus* time of the dual $BiVO_4$ photoanodes with abundant oxygen vacancies coated with FeOOH/NiOOH oxygen evolution cocatalysts at 1.23 V *versus* RHE under AM 1.5 G illumination. Reproduced from ref. 80 with permission. Copyright 2018, Wiley-VCH. (f) High resolution O 1s XPS spectra of $BiVO_4$ and 3 at% Zn doped $BiVO_4$ (3Zn-$BiVO_4$). (g) EPR curves of $BiVO_4$ with different Zn-dopant contents. (h) Schematic of the proposed band gap for the pristine $BiVO_4$/Zn-doped $BiVO_4$ homojunction photoanode. Reproduced from ref. 159 with permission. Copyright 2019, Elsevier.

(EPR) results demonstrated that with the increasing content of Zn dopant in $BiVO_4$, more oxygen vacancies are formed (Fig. 7g). As illustrated in Fig. 7h, the synergistic effect of Zn doping and oxygen vacancies not only change the conduction and valence band positions, forming a local built-in electric field, but also increase the charge carrier density, promoting charge separation and transfer. In addition, water adsorption on Bi-sites was also activated, which is also beneficial for water splitting. Interestingly, a $BiVO_4$ homojunction with abundant oxygen vacancies was prepared by a surface crystal orientation reconstruction induced by a one-step Mo doping method.[160] In addition to the generation of oxygen vacancies, Mo doping also promoted the formation of a $BiVO_4$ nanolayer with crystal orientation of (121) on the (110) facet. Compared to the pristine $BiVO_4$ photoanode, the photocurrent density of the Mo doped one is obviously improved. Similarly, Gd doping of $BiVO_4$ can also generate surface oxygen vacancies.[161]

Protecting oxygen vacancies from being oxidized during PEC water splitting is also very important to maintain the high activity and stability. Although hydrogenation treatment is a facile and efficient process to create oxygen vacancies in $BiVO_4$ photoanodes, PEC activity of the obtained oxygen deficient $BiVO_4$ photoanode would decrease due to the gradual healing of oxygen vacancies in the $BiVO_4$ photoanode. It was found that coating an ultrathin amorphous TiO_2 layer on a hydrogenated nanoporous $BiVO_4$ (H-$BiVO_4$) photoanode is effective to protect the oxygen vacancies from being oxidized during PEC water splitting.[162] Without TiO_2 coating, the photocurrent density of the H-$BiVO_4$ photoanode is decreased to the value of the pristine one after consecutive light illumination for 3 h with external bias. However, the TiO_2 coated H-$BiVO_4$ photoanode only exhibits 5% decay of the photocurrent density in the same period of time. In addition, oxygen vacancies can also be stabilized in the $BiVO_4$ Scheelite structure by incorporating Sr^{2+} to replace Bi^{3+}, resulting in the formation of corner-sharing V_2O_7 tetrahedral dimers.[163] The migration of oxygen vacancies took place through a cooperative mechanism involving V_2O_7-dimer breaking and reforming assisted by synergic rotation and deformation of the neighboring VO_4 tetrahedra.

3.1.2. Vanadium vacancies. Annealing $BiVO_4$ films at elevated temperatures without excessive vanadium sources would result in the loss of vanadium, thus forming vanadium vacancies. The loss of vanadium can be described by the following defect-chemical reactions:[133]

$$O_2(g) + V_V^{\times} + 5e' \rightarrow V_V^{''''} + VO_2(g) \quad (7)$$

$$\frac{1}{2}O_2(g) + V_V^{\times} + 5e' \rightarrow V_V^{''''} + VO(g) \quad (8)$$

$$V_V^{''''} \rightarrow V_V^{'''} + 2e' \quad (9)$$

$$2VO(g) \rightarrow VO_2(g) + V(g) \quad (10)$$

The energy level of vanadium vacancies is located at around 0.3 eV above the valence band edge of $BiVO_4$,[128] which would be deep enough in the bandgap to form trap states, rendering charge recombination centers for the photogenerated electron–hole pairs. Unlike oxygen vacancies that have positive effects on the PEC performance of $BiVO_4$ photoanodes, vanadium vacancies generally reduce the photocurrent densities. Fortunately, vanadium loss in $BiVO_4$ photoanodes can be avoided by supplying excess vanadium in the gas phase during the calcination process.[133]

Very recently, the formation of vanadium vacancies and their impact on PEC water splitting performance of the $BiVO_4$ photoanodes were systematically studied.[99] $BiVO_4$ films with a high intrinsic level of vanadium vacancies (denoted as V_V-$BiVO_4$) were prepared by high-temperature self-assembly of flame-made aerosols, followed by calcination at 450 °C for 2 h in air without the addition of any vanadium source. X-ray photoelectron spectroscopy (XPS) confirmed the presence of vanadium vacancies on the surfaces of the obtained $BiVO_4$ photoanodes, whereas photoluminescence spectroscopy revealed an increased photogenerated charge recombination efficiency. The underlying mechanism was further studied by DFT calculations, which revealed that vanadium vacancies formed a new sub-band gap level near the Fermi level of $BiVO_4$, acting as recombination centers. Thus, many more photogenerated charge carriers were recombined in the bulk of $BiVO_4$ before reaching the surfaces for the subsequent oxygen evolution reaction, leading to a very low photocurrent density.

To further confirm the detrimental effect of vanadium vacancies on the PEC performance of $BiVO_4$ photoanodes, the vanadium deficient $BiVO_4$ photoanodes were annealed in the presence of an additional vanadium source to compensate for the vanadium loss (denoted as V-treated $BiVO_4$).[99] As expected, the photocurrent density was increased by 2 times compared to its vanadium deficient counterpart in the presence of Na_2SO_3 as the hole scavenger (Fig. 8a). In addition, by surface loading the V-treated $BiVO_4$ photoanode with FeOOH/NiOOH dual cocatalysts (Fig. 8b–d), the photocurrent densities of V-treated $BiVO_4$/FeOOH/NiOOH are also much higher than those of its V_V-$BiVO_4$/FeOOH/NiOOH counterpart for PEC water splitting (Fig. 8e), which is due to the enhanced charge separation and transfer efficiencies in the V-treated $BiVO_4$ photoanode (Fig. 8f).

Based on the current understanding of vanadium vacancies, it is necessary to add excess vanadium for $BiVO_4$ films during the calcination process to achieve the highly active m-s phase while avoiding the formation of vanadium vacancies. It should be mentioned that only very few reports studied the PEC performance of $BiVO_4$ photoanodes with vanadium vacancies. Thus, more experimental and theoretical studies are still required to gain more insights into the real function of vanadium vacancies during PEC water splitting. It may be too early to conclude that vanadium vacancies are detrimental to the PEC performance of $BiVO_4$ photoanodes. Like oxygen vacancies, the location (*e.g.* in the surface or in the bulk) and quantity of vanadium vacancies may also affect the PEC performance of $BiVO_4$ photoanodes. Therefore, the development of suitable strategies to accurately control the generation of vanadium vacancies in $BiVO_4$ photoanodes should be essential to promote the further development of this field.

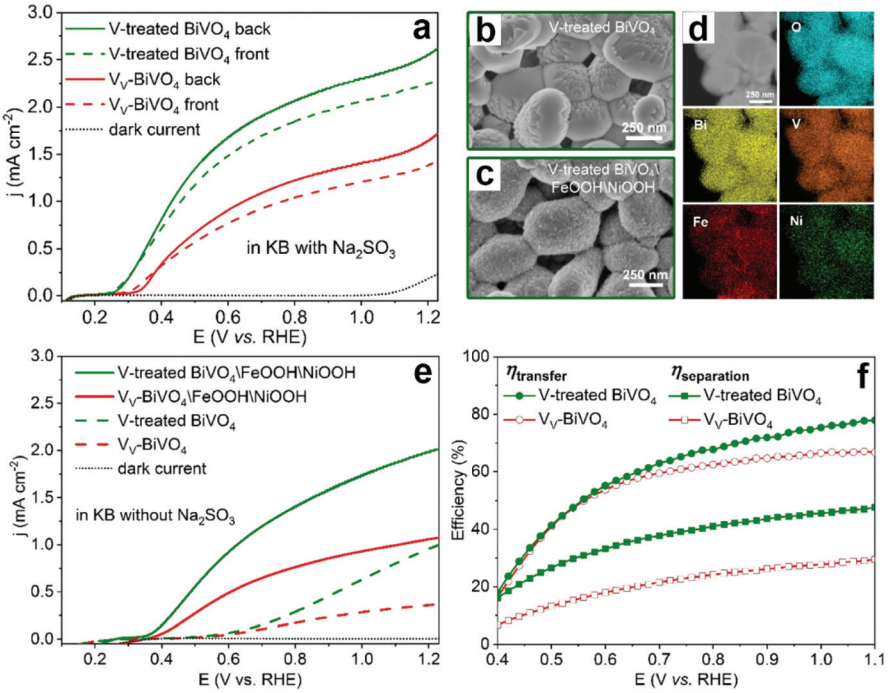

Fig. 8 (a) Photocurrent density *versus* applied potential curves of the $BiVO_4$ with vanadium vacancies (V_V-$BiVO_4$) and V-treated $BiVO_4$ photoanodes. SEM images of V-treated $BiVO_4$ (b) before and (c) after the deposition of FeOOH/NiOOH cocatalysts. (d) STEM image and elemental mapping of O, Bi, V, Fe and Ni for V-treated $BiVO_4$. (e) Photocurrent density *versus* applied potential curves of V_V-$BiVO_4$ and V-treated $BiVO_4$ with and without FeOOH/NiOOH cocatalysts. (f) Charge-transfer and charge-separation efficiencies *versus* applied potential curves of V_V-$BiVO_4$ and V-treated $BiVO_4$ photoanodes. Reproduced from ref. 99 with permission. Copyright 2021, American Chemical Society.

3.1.3. Bismuth vacancies. Interestingly, bismuth vacancies can also be generated in $BiVO_4$ photoanodes. A $BiVO_4$ (s-t) film was prepared by a solvothermal process, which was then annealed at 450 °C for 4 h in air, and a porous $BiVO_4$ (m-s) film with surface bismuth vacancies ($Bi_{1-x}VO_4$ (m-s)) was obtained (Fig. 9a and b).[96] In addition, bismuth vacancies can also be generated by doping. For instance, a solid-vapor reaction was developed to prepare fluorine-containing bismuth vanadate (F:$BiVO_4$), and it was found that the incorporation of fluorine induces the formation of cation vacancies, leading to the formation of $Bi_{0.94}V_{0.94}O_{3.54}F_{0.46}$.[164] $BiVO_4$ (t-z) films with bismuth vacancies (P-$BiVO_4$) were grown on FTO substrates by a hydrothermal process in the presence of EDTA.[97] Owing to the strong complexing ability of EDTA with Bi^{3+} ions during the hydrothermal process, bismuth vacancies were formed in the obtained $BiVO_4$ films, leading to a p-type conductivity. Interestingly, the morphologies of P-$BiVO_4$ and typical n-type $BiVO_4$ (N-$BiVO_4$) are very different (Fig. 9c and d). As expected, the P-$BiVO_4$ film exhibits cathodic photocurrent densities, while the N-$BiVO_4$ exhibits typical anodic photocurrent densities (Fig. 9e). Moreover, the Mott–Schottky plot of P-$BiVO_4$ shows a negative slope, indicating the p-type conductivity (Fig. 9f), which is different from the typical N-$BiVO_4$ film.

Compared to oxygen vacancies that have been intensively studied in $BiVO_4$ photoanodes, only a few reports mentioned bismuth vacancies in $BiVO_4$. Different from vanadium vacancies that are reported to have a detrimental effect on the PEC performance of $BiVO_4$, surface bismuth vacancies exhibit a positive effect on tuning the optoelectronic structure of $BiVO_4$, leading to an enhanced photocatalytic activity. Moreover, bismuth vacancies can also change the conductivity of $BiVO_4$ from n-type to p-type, enabling the design of an unbiased PEC water splitting system composed of only $BiVO_4$ as both the photoanode and photocathode.[98] However, the underlying mechanism of how bismuth vacancies affect the electronic structure and PEC performance of $BiVO_4$ is still unclear, which requires more efforts in the research of this field. The development of cutting-edge characterization technology and the combination of DFT calculations may gain more insights into understanding the real role of bismuth vacancies in $BiVO_4$ photoanodes.

3.2. Roles of vacancy defects in $BiVO_4$ photoanodes

During PEC water splitting, the $BiVO_4$ photoanode will absorb photons with energy higher than its bandgap under light illumination, and electrons and holes will be generated. Then, electrons will migrate to the counter electrode for the hydrogen evolution reaction (HER), while holes will transfer to the surface of $BiVO_4$ for the oxygen evolution reaction (OER). During this process, charge recombination also occurs. Vacancy defects will affect the crystal structure and electronic and optical properties of $BiVO_4$ photoanodes,[165] inducing profound impact on their PEC performances. For example, DFT calculations revealed that oxygen vacancies can change the

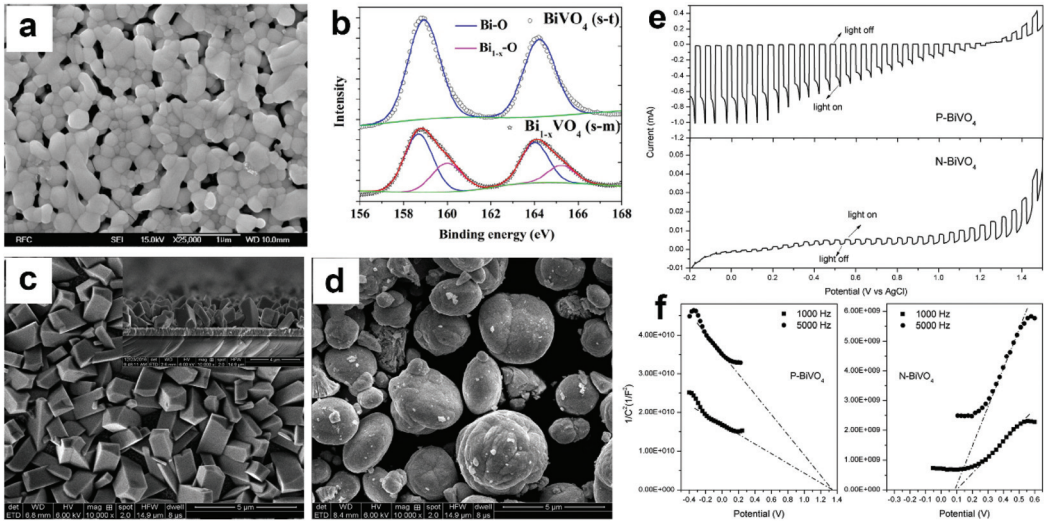

Fig. 9 (a) SEM image of $Bi_{1-x}VO_4$ (m-s). (b) High resolution Bi 4f XPS spectra of $BiVO_4$ (s-t) and $Bi_{1-x}VO_4$ (m-s). Reproduced from ref. 96 with permission. Copyright 2017, Elsevier. SEM images of (c) P-$BiVO_4$ and (d) N-$BiVO_4$. (e) Photocurrent density *versus* applied potential curves and (f) Mott–Schottky plots of the P-$BiVO_4$ and N-$BiVO_4$ photoelectrodes. Reproduced from ref. 97 with permission. Copyright 2019, Elsevier.

bandgap of $BiVO_4$ from an indirect one into a direct one, enhance the hybridization of O 2p, V 3d and Bi 6s orbitals, and shift the band edges to lower energies.[166] Considering the positive effect of vacancy defects on the design of efficient $BiVO_4$ photoanodes for PEC water splitting, it is necessary to deeply understand the roles of vacancy defects in tuning the electronic structure, promoting charge separation, and increasing surface photoreaction kinetics. In this section, we will critically discuss the main roles of vacancy defects in $BiVO_4$ photoanodes during PEC water splitting, and hope to provide new insights for the design of efficient $BiVO_4$ photoanodes for solar fuel production.

3.2.1. Tuning the electronic structure. Light absorption is the first step for PEC water splitting, which determines the maximum STH efficiency of a certain photoelectrode material. Unfortunately, most of the metal oxide semiconductors have a relatively large bandgap, leading to a narrow light absorption capacity. The generation of oxygen vacancies has been confirmed as an effective strategy to extend the light absorption range. For example, the bandgap of TiO_2 is 3.2 eV, which can only absorb ultraviolet light that accounts for 4% of the solar spectrum.[167] By annealing white TiO_2 in H_2 gas (20 bar) at 200 °C for 5 days, abundant oxygen vacancies were generated, which can enlarge the light absorption edge up to 1150 nm.[168] This pioneering work opened up new opportunities for the design of efficient metal oxide photocatalysts with narrow bandgaps. Similarly, black $BiVO_4$ (b-$BiVO_4$) films with moderate oxygen vacancies were obtained by H_2 plasma treatment, which is very different from the conventional $BiVO_4$ film with yellow color, leading to a bandgap reduction of approximately 0.3 eV that significantly enhances solar utilization (Fig. 10a).[148] By depositing an amorphous layer of TiO_{2-x} as both the oxygen evolution cocatalyst and protection layer to suppress anodic photo-corrosion of the b-$BiVO_4$, the b-$BiVO_4$/TiO_{2-x} photoanode exhibits a high and stable photocurrent density of 6.12 mA cm^{-2} at 1.23 V *versus* RHE under AM 1.5 G illumination (Fig. 10b), achieving a remarkable ABPE up to 2.5% for PEC water splitting (Fig. 10c).

In addition to light absorption, the conductivity of semiconductor films is another important factor for efficient PEC water splitting, because it significantly affects the photogenerated charge separation and transfer properties in the photoanode. As for $BiVO_4$, oxygen vacancies can increase the charge carrier density, thus improving the conductivity. For example, DFT calculations revealed that both oxygen vacancies and hydrogen impurities in the hydrogen-treated $BiVO_4$ (H-$BiVO_4$) photoanodes are shallow donors with low formation energies, which can increase the donor densities without introducing deep trap states.[147] In addition, the light absorption efficiency is improved with the increase of the hydrogen treatment temperature (Fig. 10d), which is consistent with the formation of more oxygen vacancies and hydrogen impurities, as evidenced by the considerably broader Raman peaks (Fig. 10e). Compared to pristine $BiVO_4$, the H-$BiVO_4$ exhibits a significantly smaller slope in the Mott–Schottky plot (Fig. 10f), indicating the dramatic increase of the donor density, which effectively increases the conductivity within the film. Moreover, electrochemical impedance measurements also confirm that the donor densities of $BiVO_4$ films are dramatically increased by hydrogenation. In addition, oxygen vacancies can be introduced into $BiVO_4$ photoanodes upon electrochemical reduction, which is accompanied by the formation of partial reduction of Bi^{3+} and V^{5+}.[79] The carrier concentration was improved by two times, which significantly improves the charge separation and transfer efficiency. Compared to pristine $BiVO_4$, hydrogen-treated $BiVO_4$ with oxygen vacancies (H-$BiVO_{4-x}$) exhibits a much higher photocurrent density, due to the enhanced carrier density and conductivity.[169] DFT calcu-

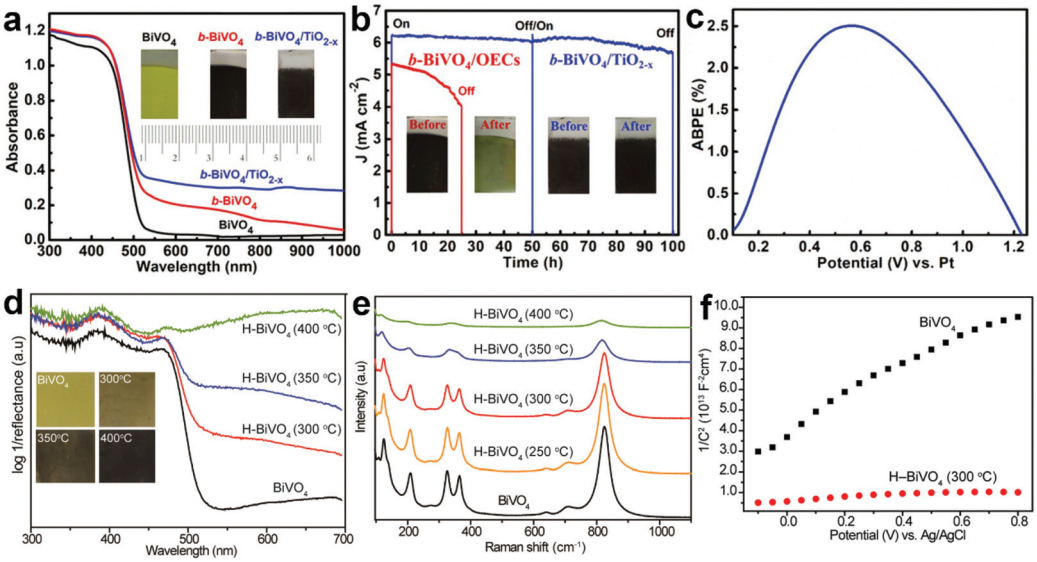

Fig. 10 (a) UV-vis absorption spectra of the $BiVO_4$, b-$BiVO_4$, and b-$BiVO_4/TiO_{2-x}$ photoanodes. Inset: digital images of the $BiVO_4$, b-$BiVO_4$, and b-$BiVO_4/TiO_{2-x}$ photoanodes. (b) Photocurrent density *versus* time plots of the b-$BiVO_4/TiO_{2-x}$ and b-$BiVO_4$/FeOOH/NiOOH photoanodes for PEC water splitting at 1.23 V *versus* RHE. (c) ABPE curve of the b-$BiVO_4/TiO_{2-x}$ photoanode obtained in a two-electrode cell for PEC water splitting. Reproduced from ref. 148 with permission. Copyright 2019, Wiley-VCH. (d) UV-vis absorption spectra of the air-annealed $BiVO_4$ film and H-$BiVO_4$ films hydrogen treated at 300, 350, and 400 °C. Inset: digital images of the air-annealed $BiVO_4$ film and H-$BiVO_4$ films. (e) Raman spectra of the air-annealed $BiVO_4$ film and H-$BiVO_4$ films hydrogen treated at 300, 350, and 400 °C. (f) Mott–Schottky plots of $BiVO_4$ and H-$BiVO_4$ (300 °C) in the dark with a frequency of 10 kHz. Reproduced from ref. 147 with permission. Copyright 2013, American Chemical Society.

lations demonstrated that the carrier concentration and mobility of $BiVO_4$ may be significantly enhanced by doping with oxygen vacancies and nitrogen impurities.[170] The underlying mechanism is that the localized electrons provided by an oxygen vacancy may be easily ionized, thus contributing to polaron carriers and n-type properties of $BiVO_4$.

3.2.2. Promoting charge separation. Efficient charge separation is essential to achieve a high PEC water splitting performance, as it determines the number of photogenerated holes reaching the surface of the $BiVO_4$ photoanode for the subsequent surface reaction. The main role of vacancy defects in $BiVO_4$ photoanodes is to promote charge separation. For example, DFT calculations revealed that oxygen vacancies were stable when incorporated into $BiVO_4$(001), which changed the V 3d orbitals by adding a new bandgap level, inducing the redundant electrons of V atoms to become carriers and promoting the separation of photogenerated electron–hole pairs.[171] Experimental results demonstrated that oxygen vacancies can significantly improve the electron mobility of $BiVO_4$ photoanodes, which promotes electron transfer and suppresses charge recombination, resulting in more photogenerated holes injecting to the electrolyte for the OER.[172] By introducing surface oxygen vacancies into $BiVO_4$ photoanodes, the charge carrier recombination was decreased, leading to a photocurrent density of 2.2 mA cm^{-2} at 1.23 V *versus* RHE under AM 1.5 G illumination, which almost doubles that of their pristine counterpart.[153] A facile photo-assisted self-reduction treatment of $BiVO_4$ photoanodes led to the partial reduction of Bi^{3+} and V^{5+} cations that generated oxygen vacancies, which increased the carrier density and charge mobility.[156] Consequently, the charge separation efficiency is improved, leading to enhanced PEC water splitting performance. Recently, dual $BiVO_4$ photoanodes with *in situ* formed oxygen vacancies in the whole film were fabricated by a sulfur oxidation process (Fig. 11A), which increases the majority charge carrier density and photovoltage (Fig. 11B), achieving a record charge separation efficiency of 98.2% (Fig. 11C).[81] As a result, an excellent photocurrent density of 6.24 mA cm^{-2} at 1.23 V *versus* RHE under AM 1.5 G illumination is obtained after loading with $NiFeO_x$ as the oxygen evolution cocatalyst (Fig. 11D), achieving a high ABPE of 2.76% (Fig. 11E).

As illustrated in Fig. 11F, oxygen vacancies play an important role in space-charge layer formation and n-type doping of bulk $BiVO_4$ to reduce resistance losses during charge transport, promoting charge separation.[173] Moreover, oxygen vacancies also participate in the trapping of photogenerated electrons and holes. In the bulk of $BiVO_4$, oxygen vacancies can trap the photogenerated holes that are energetically unable to drive water oxidation, leading to the loss of photogenerated holes. On the other hand, electron trapping is reversible, and the de-trapping activation energy is approximately 0.2 eV. Generally, electron trapping takes place in the space-charge layer, in which most oxygen vacancies are ionized in the dark, leading to a thermally activated electron extraction into the external circuit. As a result, a higher PEC water splitting performance is achieved at higher temperatures, which is essential for technological application of $BiVO_4$ photoanodes with oxygen vacancies under one sun or concentrated sunlight illumination.

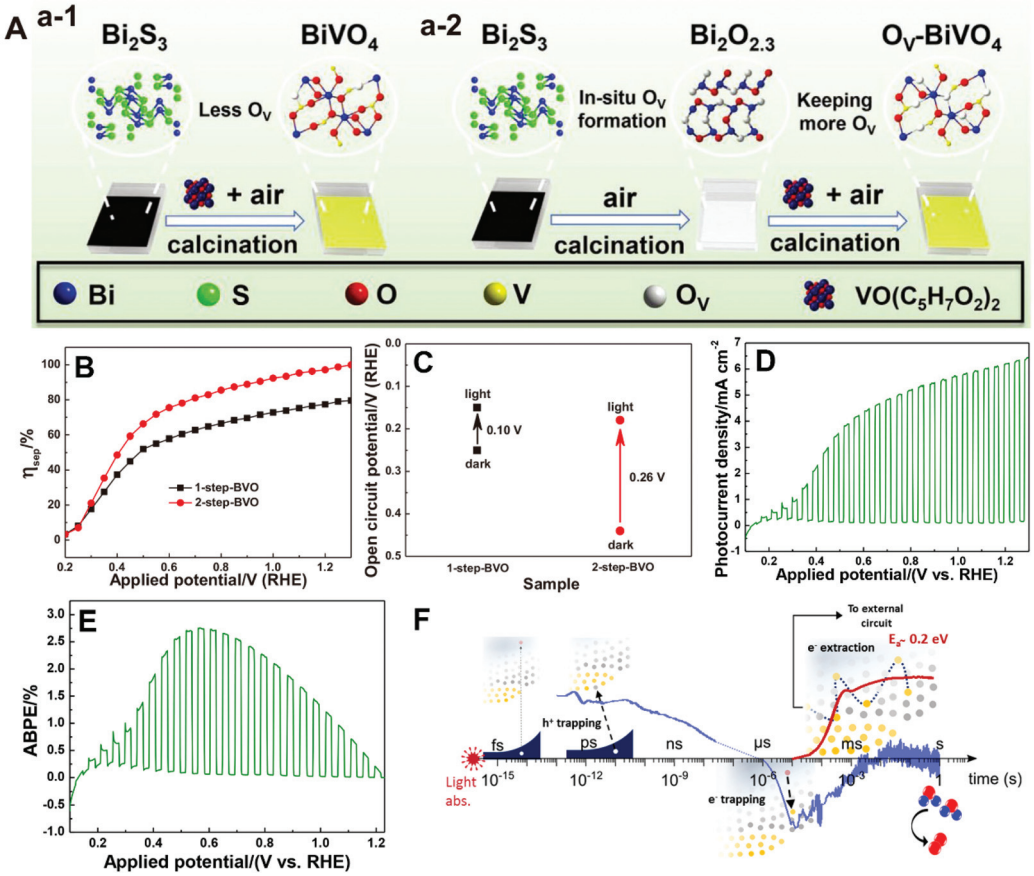

Fig. 11 (A) Schematic illustration of the fabrication of $BiVO_4$ films with (a-1) less oxygen vacancies (1-step-BVO) and (a-2) more oxygen vacancies (2-step-BVO). (B) Charge separation efficiencies and (C) open-circuit potential under AM 1.5 G illumination of one-step-BVO and two-step-BVO photoanodes. (D) Photocurrent density *versus* potential and (E) ABPE curve of dual 2-step-BVO/$NiFeO_x$ photoanodes. Reproduced from ref. 81 with permission. Copyright 2020, Wiley-VCH. (F) Schematic illustration of the role of oxygen vacancies in charge carrier trapping and electron transport in $BiVO_4$ from the time scale of light absorption to water oxidation. Reproduced from ref. 173 with permission. Copyright 2019, American Chemical Society.

3.2.3. Increasing surface photoreaction kinetics. The surface photoreaction is the last step during PEC water splitting, which is affected by the adsorption of water molecules and the reaction kinetics. Generally, oxygen evolution cocatalysts would be loaded on the surface of $BiVO_4$ photoanodes to accelerate the surface photoreaction. It has been widely accepted that oxygen vacancies in the electrocatalyst can promote the reaction kinetics, which is also effective in PEC water splitting. For example, the incorporation of Fe into CoO_x generated abundant oxygen vacancies in $FeCoO_x$ and constructed a p–n heterojunction with $BiVO_4$, thus promoting the transfer of photogenerated holes from $BiVO_4$ and reducing the overpotential for the OER (Fig. 12a and b).[174] As a result, a high photocurrent density of 4.82 mA m^{-2} at 1.23 V *versus* RHE under AM 1.5 G illumination was achieved, which is over 2 times higher than that of the pristine $BiVO_4$ photoanode (Fig. 12c). In addition, surface oxygen vacancies in $BiVO_4$ materials can also increase surface photoreaction kinetics. DFT calculations revealed that oxygen vacancies in $BiVO_4$ are deep donors at the surface as they are in the bulk, which may be beneficial for adsorption.[175,176] In addition, surface oxygen vacancies played a pivotal role in charge transfer mechanisms when coupled with the oxygen evolution cocatalyst, promoting PEC water splitting reactions. Thus, the functions of oxygen vacancies in the bulk and at the surface are different, which should be taken into account for the in-depth understanding of PEC water splitting of $BiVO_4$ photoanodes.

DFT calculations also suggested that the V site is the active site for PEC water splitting in $BiVO_4$ photoanodes, and the number of active sites is significantly increased by the formation of oxygen vacancies.[177] Compared to pristine $BiVO_4$ photoanodes, the adsorption energies for H_2O_{ads}, OH_{ads}, and O_{ads} are higher in the oxygen vacancy enriched one (Fig. 12d), indicating the enhanced hole transfer efficiency from the photoanode surface to the electrolyte for the OER. These DFT calculation results are consistent with the experimental results.[178] A multi-cycle electrodeposition process followed by high-temperature annealing was developed to prepare multilayer $BiVO_4$ photoanodes with abundant oxygen vacancies and V^{4+} in the crystal lattice, which promotes mass and charge

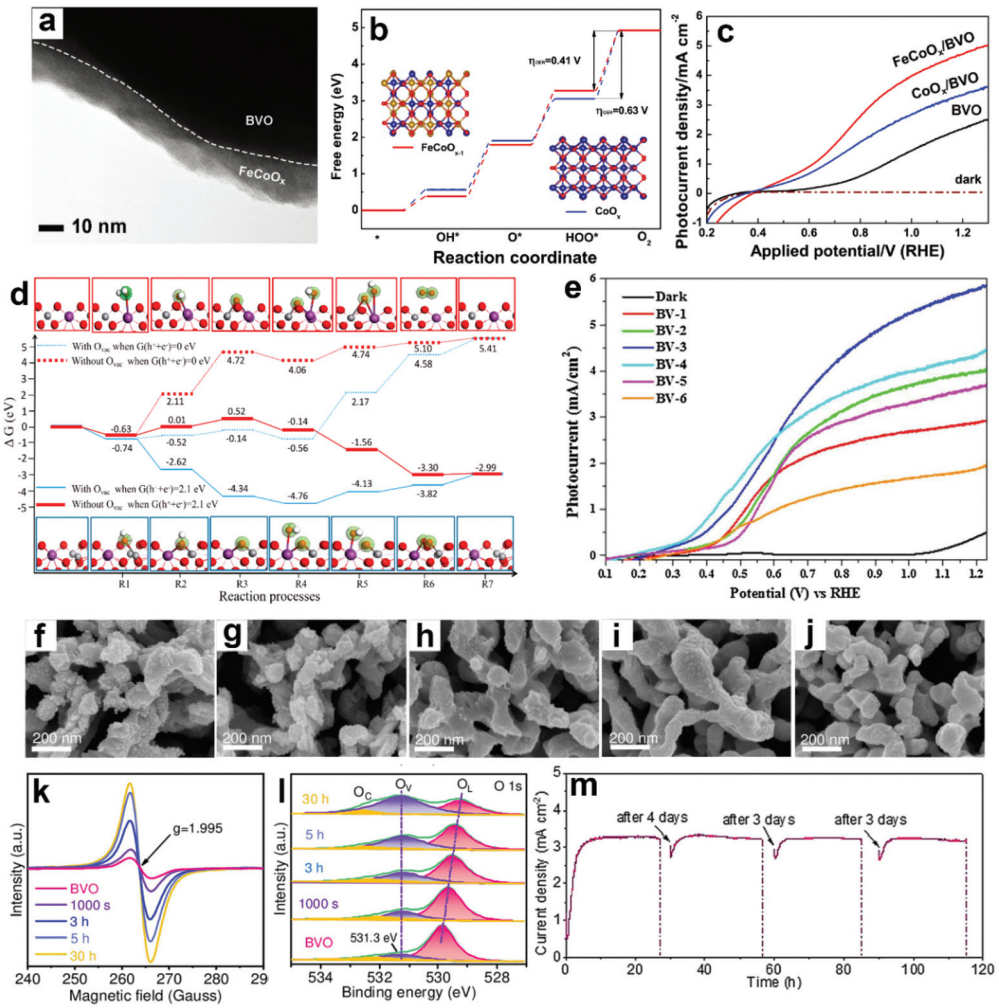

Fig. 12 (a) TEM image of $BiVO_4$ coated with $FeCoO_x$ as the oxygen evolution cocatalyst ($FeCoO_x$/BVO). (b) Free energy diagram of CoO_x and $FeCoO_{x-1}$ (*i.e.*, $FeCoO_x$ with oxygen vacancies) for the OER pathway. Insets: the models of $FeCoO_{x-1}$ (left) and CoO_x (right): blue spheres: Co atoms, gold spheres: Fe atoms, and red spheres: O atoms. (c) Photocurrent density *versus* applied potential curves. Reproduced from ref. 174 with permission. Copyright 2018, Wiley-VCH. (d) Free energy diagram of the OER on $BiVO_4$ (010) facets and $BiVO_4$ (010) facets with oxygen vacancies. Reproduced from ref. 177 with permission. Copyright 2017, American Chemical Society. (e) Photocurrent density *versus* applied potential curves for sulfite oxidation under light illumination (100 mW cm^{-2}). Reproduced from ref. 179 with permission. Copyright 2017, Elsevier. Characteristics of $BiVO_4$ photoanodes potentiostatically photopolarized at 0.8 V *versus* RHE as a function of time (0 s, 1000 s, 3 h, 5 h, and 30 h) under AM 1.5 G (100 mA cm^{-2}) illumination: SEM images of samples for (f) 0 s, (g) 1000 s, (h) 3 h, (i) 5 h, (j) 30 h. (k) EPR spectra. (l) High-resolution O 1s XPS peak. (m) Cycling photostability of $BiVO_4$ photoanodes potentiostatically photopolarized at 0.8 V *versus* RHE in 1 M KBi (pH 9.5). Reproduced from ref. 94 with permission. Copyright 2020, Wiley-VCH.

transfer, leading to a photocurrent density of 5.80 mA cm^{-2} in sulfite oxidation at 1.23 V *versus* RHE under AM 1.5 G illumination (Fig. 12e).[179] By incorporating nitrogen into $BiVO_4$ photoanodes, oxygen vacancies and V^{5+}/V^{4+} redox channels were generated, which diminished surface recombination, promoting the injection of photogenerated holes into the electrolyte for the OER.[180]

It was found that oxygen vacancies can directly enhance OER reactivity by tailoring coordination of surface metal sites in $BiVO_4$ photoanodes.[149] In the presence of oxygen vacancies, the optimized surface catalytic kinetics significantly promote the surface reaching holes for the OER on the photoanode surface without any oxygen evolution cocatalysts, exhibiting a high photocurrent density of 4.32 mA cm^{-2} at 1.23 V *versus* RHE under AM 1.5 G illumination. Similarly, a potentiostatically photopolarized process generated surface oxygen vacancies in $BiVO_4$ photoanodes.[94] By tuning the potentiostatic photopolarization time, porous $BiVO_4$ photoanodes with different numbers of oxygen vacancies were obtained (Fig. 12f–l). Without any oxygen evolution cocatalysts, the obtained $BiVO_4$ photoanode exhibited a record-high photocurrent density of 4.60 mA cm^{-2} at 1.23 V *versus* RHE with a low onset potential of 0.23 V *versus* RHE in a borate buffer electrolyte without any sacrificial agent under AM 1.5 G illumination. Impressively, an excellent photostability of over 100 h was achieved under the intermittent test (Fig. 12m). These very

encouraging works demonstrate the excellent cocatalyst-like function of oxygen vacancies, which may inspire the design of efficient cocatalyst-free $BiVO_4$ photoanodes for PEC water splitting.

4. Conclusion and outlook

$BiVO_4$ is one of the most promising photoanode materials for PEC water splitting, and has attracted great attention in recent years. With the in-depth theoretical understanding on the material design and the development of cutting-edge time-resolve technologies, great breakthroughs have been achieved. The record photocurrent density of the $BiVO_4$ single junction photoanode is 6.24 mA cm^{-2} at 1.23 V *versus* RHE under AM 1.5 G illumination in the presence of oxygen vacancies and the $NiFeO_x$ cocatalyst,[81] whereas the $WO_3/BiVO_4$/Co–Pi heterojunction photoanode can achieve a record photocurrent density of 6.72 mA cm^{-2} at 1.23 V *versus* RHE under AM 1.5 G illumination.[181] Since the theoretical photocurrent density of $BiVO_4$ photoanodes is 7.5 mA cm^{-2} under AM 1.5 G illumination, the experimental values achieved indicate the superior PEC performance of $BiVO_4$ compared to other photoanode materials. Recently, vacancy defect engineering has stood out to be an efficient strategy to tailor the optoelectronic properties of $BiVO_4$ photoanodes, which has attracted increasing attention. This review article briefly introduces the fundamental properties of $BiVO_4$ including crystal structure, optical properties, carrier transport and photogenerated carrier lifetime. Then, emerging strategies to generate vacancy defects including oxygen vacancies, vanadium vacancies and bismuth vacancies in $BiVO_4$ photoanodes are systematically presented. Finally, the roles of vacancy defects in $BiVO_4$ photoanodes in terms of tuning the electronic structure, promoting charge separation, and increasing surface photoreaction kinetics are critically discussed.

Although great achievements have been made for vacancy defect engineering of $BiVO_4$ photoanodes, some emerging challenges should not be ignored. For example, most of the reports confirmed the positive effect of oxygen vacancies for $BiVO_4$ photoanodes. However, recent DFT calculations revealed that neutral oxygen vacancies not only apparently decrease the bandgap but also cause localized lattice distortions by forming stable V–O–V bonds and localize electrons in V^{5+} atoms by forming V^{4+} small polarons, which act as recombination centers and dramatically accelerate the nonradiative electron recombination by a factor of approximately 1100 compared to that of the pristine one.[182] Therefore, in-depth understanding of the formation of oxygen vacancies and their effect on the optoelectronic properties of $BiVO_4$ photoanodes is still required. In addition, $BiVO_4$ exhibits facet-dependent PEC water splitting performance, so oxygen vacancies on different facets of $BiVO_4$ may show different PEC performance. How to selectively generate oxygen vacancies on different facets of $BiVO_4$ is challenging while worth investigating. Many reports have shown the different roles of oxygen vacancies at the surface and in the bulk of $BiVO_4$ photoanodes. How to control the oxygen vacancies in different locations of the $BiVO_4$ film is another challenging task. On the other hand, excessive oxygen vacancies generally show a detrimental effect on the PEC performance of $BiVO_4$; is it possible to quantitatively control the oxygen vacancies? The development of cutting-edge technologies may provide a reliable way for the quantitative analysis of oxygen vacancies. With the development of knowledge to deeply understand the formation of oxygen vacancies, maybe we can develop a reliable approach to quantitatively control the oxygen vacancies in $BiVO_4$ photoanodes. Compared to oxygen vacancies, very few reports investigated other defects such as vanadium or bismuth defects in $BiVO_4$ photoanodes. How to control the type, location and quantity of these kinds of defects is another question. In addition, the multiple-effect roles of vacancy defects in the three main PEC processes are difficult to be decoupled for better analysis, which is challenging for the further development of vacancy defect engineering of $BiVO_4$ photoanodes. Considering that the photocurrent densities of $BiVO_4$ photoanodes are already very close to the theoretical maximum, to further improve the PEC performance of $BiVO_4$, the next step should be the effective reduction of its bandgap. How to reduce the bandgap of $BiVO_4$ while keeping the high charge separation and transfer properties through vacancy defect engineering is also very challenging.

Owing to the suitable band edge positions and the relatively narrow bandgap for visible light absorption, $BiVO_4$ photoanodes are very promising for unbiased PEC water splitting when coupled with another photocathode or photovoltaic (PV) device. For example, connecting the $WO_3/BiVO_4$/Co–Pi heterojunction photoanode with a double-junction GaAs/InGaAsP photovoltaic cell can achieve a STH efficiency of 8.1%.[181] In spite of the high STH efficiency, the utilization of the double-junction GaAs/InGaAsP photovoltaic cell is extremely expensive, which should be taken into account for possible practical applications. With the rapid development of low-cost metal halide perovskite solar cells, coupling $BiVO_4$ photoanodes with perovskite solar cells may be a good choice to keep the high STH efficiency while reducing the cost. Our group developed a wireless device composed of the oxygen vacancy enriched $BiVO_4$/FeOOH/NiOOH dual photoanodes and a single sealed perovskite solar cell, leading to a STH efficiency of 6.5%.[80] The long-term stability of this device is mainly determined by the perovskite solar cell. Compared to the $BiVO_4$-PV system, the $BiVO_4$-photocathode system is more desirable for possible practical applications due to the much lower cost. By coupling the $BiVO_4$ photoanode with a Cu_2O photocathode, a STH efficiency of 3% is achieved.[183] In addition, a standalone overall solar water splitting system composed of a $BiVO_4$ photoanode and a Cu_2ZnSnS_4 photocathode exhibited a higher STH efficiency of 3.17%.[184] Very recently, an integrated system composed of a $BiVO_4$ photoanode and an organic polymer-based photocathode (PBDB-T:ITIC:PC71BM) made a new breakthrough of the STH efficiency to 4.3%.[185] Therefore, with the development of a more efficient photocathode, the STH efficiency of the $BiVO_4$ photoanode coupled with another

photocathode to construct an unbiased PEC water splitting system can be further improved. Possibly, the combination of vacancy defect engineering with other state-of-the-art strategies can develop both an efficient $BiVO_4$ photoanode and photocathode, leading to a new breakthrough of the STH efficiency, thus promoting the PEC water splitting technology a step closer to practical applications. We wish to see more exciting development of efficient $BiVO_4$ photoanodes upon vacancy defect engineering in the near future.

Conflicts of interest

There are no conflicts of interest to declare.

Acknowledgements

The authors would like to acknowledge the financial support from National Natural Science Foundation of China (No. 52002328), the Fundamental Research Funds for the Central Universities, the Joint Research Funds of Department of Science & Technology of Shaanxi Province and Northwestern Polytechnical University (2020GXLH-Z-018), and Australian Research Council through its Discovery Projects (DPs) and Laureate Fellowship.

References

1 Z.-j. Wang, H. Song, H. Liu and J. Ye, *Angew. Chem., Int. Ed.*, 2020, **59**, 8016–8035.
2 Z.-H. Zhou, K.-H. Chen, S. Gao, Z.-W. Yang and L.-N. He, *Research*, 2020, **2020**, 9398285.
3 M.-q. Cao, K. Liu, H.-m. Zhou, H.-m. Li, X.-h. Gao, X.-q. Qiu and M. Liu, *J. Cent. South Univ.*, 2019, **26**, 1503–1509.
4 P. Wang, S. Wang, H. Wang, Z. Wu and L. Wang, *Part. Part. Syst. Charact.*, 2018, **35**, 1700371.
5 Z. Sun and Z.-q. Sun, *J. Cent. South Univ.*, 2020, **27**, 1074–1103.
6 M. Z. Jacobson, M. A. Delucchi, Z. A. F. Bauer, S. C. Goodman, W. E. Chapman, M. A. Cameron, C. Bozonnat, L. Chobadi, H. A. Clonts, P. Enevoldsen, J. R. Erwin, S. N. Fobi, O. K. Goldstrom, E. M. Hennessy, J. Liu, J. Lo, C. B. Meyer, S. B. Morris, K. R. Moy, P. L. O'Neill, I. Petkov, S. Redfern, R. Schucker, M. A. Sontag, J. Wang, E. Weiner and A. S. Yachanin, *Joule*, 2017, **1**, 108–121.
7 Y. Qiu, Z. Pan, H. Chen, D. Ye, L. Guo, Z. Fan and S. Yang, *Sci. Bull.*, 2019, **64**, 1348–1380.
8 Z. Luo, T. Wang and J. Gong, *Chem. Soc. Rev.*, 2019, **48**, 2158–2181.
9 D. K. Lee, D. Lee, M. A. Lumley and K. S. Choi, *Chem. Soc. Rev.*, 2019, **48**, 2126–2157.
10 Y. He, T. Hamann and D. Wang, *Chem. Soc. Rev.*, 2019, **48**, 2182–2215.
11 K. Sivula and R. van de Krol, *Nat. Rev. Mater.*, 2016, **1**, 15010.
12 B. Liu, S. Feng, L. Yang, C. Li, Z. Luo, T. Wang and J. Gong, *Energy Environ. Sci.*, 2020, **13**, 221–228.
13 S. Wang and L. Wang, *Tungsten*, 2019, **1**, 19–45.
14 W. Wang, M. Xu, X. Xu, W. Zhou and Z. Shao, *Angew. Chem., Int. Ed.*, 2020, **59**, 136–152.
15 T. Hisatomi, J. Kubota and K. Domen, *Chem. Soc. Rev.*, 2014, **43**, 7520–7535.
16 C. Jiang, S. J. A. Moniz, A. Wang, T. Zhang and J. Tang, *Chem. Soc. Rev.*, 2017, **46**, 4645–4660.
17 T. Yao, X. An, H. Han, J. Q. Chen and C. Li, *Adv. Energy Mater.*, 2018, **8**, 1800210.
18 A. Riapanitra, Y. Asakura and S. Yin, *Tungsten*, 2019, **1**, 306–317.
19 S. Wang, H. Chen, G. Gao, T. Butburee, M. Lyu, S. Thaweesak, J.-H. Yun, A. Du, G. Liu and L. Wang, *Nano Energy*, 2016, **24**, 94–102.
20 T. Butburee, Y. Bai, H. Wang, H. Chen, Z. Wang, G. Liu, J. Zou, P. Khemthong, G. Q. Lu and L. Wang, *Adv. Mater.*, 2018, **30**, 1705666.
21 P. Peerakiatkhajohn, J.-H. Yun, H. Chen, M. Lyu, T. Butburee and L. Wang, *Adv. Mater.*, 2016, **28**, 6405–6410.
22 S. Wang, L. Wang and W. Huang, *J. Mater. Chem. A*, 2020, **8**, 24307–24352.
23 P. Liu, C. Wang, L. Wang, X. Wu, L. Zheng and H. G. Yang, *Research*, 2020, **2020**, 5473217.
24 S. Wang, F. Tang and L. Wang, *J. Inorg. Mater.*, 2018, **33**, 173–197.
25 X. Zou, Z. Sun and Y. H. Hu, *J. Mater. Chem. A*, 2020, **8**, 21474–21502.
26 Y. Yang, S. Wang, Y. Jiao, Z. Wang, M. Xiao, A. Du, Y. Li, J. Wang and L. Wang, *Adv. Funct. Mater.*, 2018, **28**, 1805698.
27 R. Chen, C. Zhen, Y. Yang, X. Sun, J. T. S. Irvine, L. Wang, G. Liu and H.-M. Cheng, *Nano Energy*, 2019, **59**, 683–688.
28 M. Higashi, K. Domen and R. Abe, *J. Am. Chem. Soc.*, 2012, **134**, 6968–6971.
29 G. Liu, S. Ye, P. Yan, F. Xiong, P. Fu, Z. Wang, Z. Chen, J. Shi and C. Li, *Energy Environ. Sci.*, 2016, **9**, 1327–1334.
30 X. Wang, B. Liu, X. Xiao, S. Wang and W. Huang, *J. Mater. Chem. C*, 2021, DOI: 10.1039/D1TC04142H.
31 S. Wang, Y. Li, X. Wang, G. Zi, C. Zhou, B. Liu, G. Liu, L. Wang and W. Huang, *J. Mater. Sci. Technol.*, 2022, **104**, 155–162.
32 R. Liu, H.-L. Fei and G.-L. Ye, *Tungsten*, 2020, **2**, 147–161.
33 K. Matoba, M. Takahashi, Y. Matsuda and S. Higashimoto, *J. Electroanal. Chem.*, 2021, **895**, 115489.
34 C.-B. Sun, Y.-W. Zhong, W.-J. Fu, Z.-Q. Zhao, J. Liu, J. Ding, X.-P. Han, Y.-D. Deng, W.-B. Hu and C. Zhong, *Tungsten*, 2020, **2**, 109–133.
35 K. Feng, D. Huang, L. Li, K. Wang, J. Li, T. Harada, S. Ikeda and F. Jiang, *Appl. Catal., B*, 2020, **268**, 118438.
36 C. T. Altaf, N. S. Sahsuvar, N. Abdullayeva, O. Coskun, A. Kumtepe, E. Karagoz, M. Sankir and N. D. Sankir, *ACS Sustainable Chem. Eng.*, 2020, **8**, 15209–15222.

37 J. Ke, F. He, H. Wu, S. Lyu, J. Liu, B. Yang, Z. Li, Q. Zhang, J. Chen, L. Lei, Y. Hou and K. Ostrikov, *Nano-Micro Lett.*, 2021, **13**, 24.
38 F. Zhang, Z. Ma, Z. Shi, X. Chen, D. Wu, X. Li and C. Shan, *Energy Mater. Adv.*, 2021, **2021**, 5198145.
39 J. Chen, C. Dong, H. Idriss, O. F. Mohammed and O. M. Bakr, *Energy Material Advances*, 2020, **10**, 1902433.
40 J. Yuan, H. Liu, S. Wang and X. Li, *Nanoscale*, 2021, **13**, 10281–10304.
41 M. Crespo-Quesada, L. M. Pazos-Outón, J. Warnan, M. F. Kuehnel, R. H. Friend and E. Reisner, *Nat. Commun.*, 2016, **7**, 12555.
42 A. Fujishima and K. Honda, *Nature*, 1972, **238**, 37–38.
43 K. Zhang, B. Jin, C. Park, Y. Cho, X. Song, X. Shi, S. Zhang, W. Kim, H. Zeng and J. H. Park, *Nat. Commun.*, 2019, **10**, 2001.
44 K. H. Ye, H. Li, D. Huang, S. Xiao, W. Qiu, M. Li, Y. Hu, W. Mai, H. Ji and S. Yang, *Nat. Commun.*, 2019, **10**, 3687.
45 W. T. Qiu, S. Xiao, J. W. Ke, Z. Wang, S. T. Tang, K. Zhang, W. Qian, Y. C. Huang, D. Huang, Y. X. Tong and S. H. Yang, *Angew. Chem., Int. Ed.*, 2019, **58**, 19087–19095.
46 X. Ning, B. Lu, Z. Zhang, P. Du, H. Ren, D. Shan, J. Chen, Y. Gao and X. Lu, *Angew. Chem., Int. Ed.*, 2019, **58**, 16800–16805.
47 Q. Meng, B. Zhang, L. Fan, H. Liu, M. Valvo, K. Edstrom, M. Cuartero, R. De Marco, G. A. Crespo and L. Sun, *Angew. Chem., Int. Ed.*, 2019, **58**, 19027–19033.
48 Y. Park, K. J. McDonald and K. S. Choi, *Chem. Soc. Rev.*, 2013, **42**, 2321–2337.
49 A. Kudo, K. Ueda, H. Kato and I. Mikami, *Catal. Lett.*, 1998, **53**, 229–230.
50 K. Sayama, A. Nomura, Z. Zou, R. Abe, Y. Abe and H. Arakawa, *Chem. Commun.*, 2003, 2908–2909.
51 S. K. Pilli, T. E. Furtak, L. D. Brown, T. G. Deutsch, J. A. Turner and A. M. Herring, *Energy Environ. Sci.*, 2011, **4**, 5028–5034.
52 D. K. Zhong, S. Choi and D. R. Gamelin, *J. Am. Chem. Soc.*, 2011, **133**, 18370–18377.
53 K. J. McDonald and K.-S. Choi, *Energy Environ. Sci.*, 2012, **5**, 8553.
54 F. F. Abdi, L. Han, A. H. M. Smets, M. Zeman, B. Dam and R. van de Krol, *Nat. Commun.*, 2013, **4**, 2195.
55 X. Xu, S. Jin, C. Yang, J. Pan, W. Du, J. Hu, H. Zeng and Y. Zhou, *Sol. RRL*, 2019, **3**, 1900115.
56 S. Wang, J.-H. Yun, B. Luo, T. Butburee, P. Peerakiatkhajohn, S. Thaweesak, M. Xiao and L. Wang, *J. Mater. Sci. Technol.*, 2017, **33**, 1–22.
57 H. Ren, T. Dittrich, H. Ma, J. N. Hart, S. Fengler, S. Chen, Y. Li, Y. Wang, F. Cao, M. Schieda, Y. H. Ng, Z. Xie, X. Bo, P. Koshy, L. R. Sheppard, C. Zhao and C. C. Sorrell, *Adv. Mater.*, 2019, **31**, 1807204.
58 Y. Zhou, L. Zhang, L. Lin, B. R. Wygant, Y. Liu, Y. Zhu, Y. Zheng, C. B. Mullins, Y. Zhao, X. Zhang and G. Yu, *Nano Lett.*, 2017, **17**, 8012–8017.
59 M. Zhong, T. Hisatomi, Y. Kuang, J. Zhao, M. Liu, A. Iwase, Q. Jia, H. Nishiyama, T. Minegishi, M. Nakabayashi, N. Shibata, R. Niishiro, C. Katayama, H. Shibano, M. Katayama, A. Kudo, T. Yamada and K. Domen, *J. Am. Chem. Soc.*, 2015, **137**, 5053–5060.
60 Y. Kuang, Q. Jia, G. Ma, T. Hisatomi, T. Minegishi, H. Nishiyama, M. Nakabayashi, N. Shibata, T. Yamada, A. Kudo and K. Domen, *Nat. Energy*, 2016, **2**, 16191.
61 K.-H. Ye, Z. Wang, J. Gu, S. Xiao, Y. Yuan, Y. Zhu, Y. Zhang, W. Mai and S. Yang, *Energy Environ. Sci.*, 2017, **10**, 772–779.
62 Y. Shi, Y. Yu, Y. Yu, Y. Huang, B. Zhao and B. Zhang, *ACS Energy Lett.*, 2018, **3**, 1648–1654.
63 Q. Shi, S. Murcia-López, P. Tang, C. Flox, J. R. Morante, Z. Bian, H. Wang and T. Andreu, *ACS Catal.*, 2018, **8**, 3331–3342.
64 W. J. Jo, J.-W. Jang, K.-j. Kong, H. J. Kang, J. Y. Kim, H. Jun, K. P. S. Parmar and J. S. Lee, *Angew. Chem., Int. Ed.*, 2012, **51**, 3147–3151.
65 T. W. Kim, Y. Ping, G. A. Galli and K.-S. Choi, *Nat. Commun.*, 2015, **6**, 8769.
66 T. W. Kim and K. S. Choi, *Science*, 2014, **343**, 990–994.
67 Y. Kuang, Q. Jia, H. Nishiyama, T. Yamada, A. Kudo and K. Domen, *Adv. Energy Mater.*, 2016, **6**, 1501645.
68 Y. Qiu, W. Liu, W. Chen, W. Chen, G. Zhou, P.-C. Hsu, R. Zhang, Z. Liang, S. Fan, Y. Zhang and Y. Cui, *Sci. Adv.*, 2016, **2**, e1501764.
69 T. Li, J. He, B. Peña and C. P. Berlinguette, *Angew. Chem., Int. Ed.*, 2016, **55**, 1769–1772.
70 B. J. Trześniewski and W. A. Smith, *J. Mater. Chem. A*, 2016, **4**, 2919–2926.
71 E. Y. Liu, J. E. Thorne, Y. He and D. Wang, *ACS Appl. Mater. Interfaces*, 2017, **9**, 22083–22087.
72 B. J. Trześniewski, I. A. Digdaya, T. Nagaki, S. Ravishankar, I. Herraiz-Cardona, D. A. Vermaas, A. Longo, S. Gimenez and W. A. Smith, *Energy Environ. Sci.*, 2017, **10**, 1517–1529.
73 B. Lamm, B. J. Trześniewski, H. Döscher, W. A. Smith and M. Stefik, *ACS Energy Lett.*, 2018, **3**, 112–124.
74 M. Tayebi, A. Tayyebi and B.-K. Lee, *Sol. Energy*, 2019, **191**, 427–434.
75 H. S. Han, S. Shin, D. H. Kim, I. J. Park, J. S. Kim, P.-S. Huang, J.-K. Lee, I. S. Cho and X. Zheng, *Energy Environ. Sci.*, 2018, **11**, 1299–1306.
76 P. Li, X. Chen, H. He, X. Zhou, Y. Zhou and Z. Zou, *Adv. Mater.*, 2018, **30**, 1703119.
77 J. Song, M. J. Seo, T. H. Lee, Y.-R. Jo, J. Lee, T. L. Kim, S.-Y. Kim, S.-M. Kim, S. Y. Jeong, H. An, S. Kim, B. H. Lee, D. Lee, H. W. Jang, B.-J. Kim and S. Lee, *ACS Catal.*, 2018, **8**, 5952–5962.
78 S. Wang, G. Liu and L. Wang, *Chem. Rev.*, 2019, **119**, 5192–5247.
79 S. Wang, P. Chen, J. H. Yun, Y. Hu and L. Wang, *Angew. Chem., Int. Ed.*, 2017, **56**, 8500–8504.
80 S. Wang, P. Chen, Y. Bai, J.-H. Yun, G. Liu and L. Wang, *Adv. Mater.*, 2018, **30**, 1800486.
81 S. Wang, T. He, P. Chen, A. Du, K. Ostrikov, W. Huang and L. Wang, *Adv. Mater.*, 2020, **32**, 2001385.

82 J.-B. Pan, B.-H. Wang, J.-B. Wang, H.-Z. Ding, W. Zhou, X. Liu, J.-R. Zhang, S. Shen, J.-K. Guo, L. Chen, C.-T. Au, L.-L. Jiang and S.-F. Yin, *Angew. Chem., Int. Ed.*, 2021, **60**, 1433–1440.
83 Z.-F. Huang, L. Pan, J.-J. Zou, X. Zhang and L. Wang, *Nanoscale*, 2014, **6**, 14044–14063.
84 S. Chen, D. Huang, P. Xu, X. Gong, W. Xue, L. Lei, R. Deng, J. Li and Z. Li, *ACS Catal.*, 2020, **10**, 1024–1059.
85 J. H. Kim and J. S. Lee, *Adv. Mater.*, 2019, **31**, 1806938.
86 S. Bai, N. Zhang, C. Gao and Y. Xiong, *Nano Energy*, 2018, **53**, 296–336.
87 D. Maarisetty and S. S. Baral, *J. Mater. Chem. A*, 2020, **8**, 18560–18604.
88 L. Ran, J. Hou, S. Cao, Z. Li, Y. Zhang, Y. Wu, B. Zhang, P. Zhai and L. Sun, *Sol. RRL*, 2020, **4**, 1900487.
89 P. Raizada, V. Soni, A. Kumar, P. Singh, A. A. P. Khan, A. M. Asiri, V. K. Thakur and V.-H. Nguyen, *J. Materiomics*, 2021, **7**, 388–418.
90 S. A. Monny, Z. Wang, T. Lin, P. Chen, B. Luo and L. Wang, *Chem. Commun.*, 2020, **56**, 9376–9379.
91 Z. Wang, X. Mao, P. Chen, M. Xiao, S. A. Monny, S. Wang, M. Konarova, A. Du and L. Wang, *Angew. Chem., Int. Ed.*, 2019, **58**, 1030–1034.
92 Z. Wang, L. Zhang, T. U. Schülli, Y. Bai, S. A. Monny, A. Du and L. Wang, *Angew. Chem., Int. Ed.*, 2019, **58**, 17604–17609.
93 K. R. Tolod, S. Hernández, M. Castellino, F. A. Deorsola, E. Davarpanah and N. Russo, *Int. J. Hydrogen Energy*, 2020, **45**, 605–618.
94 R.-T. Gao and L. Wang, *Angew. Chem., Int. Ed.*, 2020, **59**, 23094–23099.
95 S. Feng, T. Wang, B. Liu, C. Hu, L. Li, Z.-J. Zhao and J. Gong, *Angew. Chem., Int. Ed.*, 2020, **59**, 2044–2048.
96 A. Tayyebi, T. Soltani, H. Hong and B.-K. Lee, *J. Colloid Interface Sci.*, 2018, **514**, 565–575.
97 J. Wang, Y. Song, J. Hu, Y. Li, Z. Wang, P. Yang, G. Wang, Q. Ma, Q. Che, Y. Dai and B. Huang, *Appl. Catal., B*, 2019, **251**, 94–101.
98 X. Liang, P. Wang, F. Tong, X. Liu, C. Wang, M. Wang, Q. Zhang, Z. Wang, Y. Liu, Z. Zheng, Y. Dai and B. Huang, *Adv. Funct. Mater.*, 2021, **31**, 2008656.
99 T. Tran-Phu, Z. Fusco, I. D. Bernardo, J. Lipton-Duffin, C. Y. Toe, R. Daiyan, T. Gengenbach, C.-H. Lin, R. Bo, H. T. Nguyen, G. M. J. Barca, T. Wu, H. Chen, R. Amal and A. Tricoli, *Chem. Mater.*, 2021, **33**, 3553–3565.
100 L. Hao, H. Huang, Y. Zhang and T. Ma, *Adv. Funct. Mater.*, 2021, **31**, 2100919.
101 Wendusu, T. Honda, T. Masui and N. Imanaka, *RSC Adv.*, 2013, **3**, 24941–24945.
102 X. Zhang, T. Chen, Y. Xu, W. Jiang, J. Liu and Z. Xie, *J. Sol-Gel Sci. Technol.*, 2019, **91**, 127–137.
103 D. T. T. Trinh, W. Khanitchaidecha, D. Channei and A. Nakaruk, *Res. Chem. Intermed.*, 2019, **45**, 5217–5259.
104 J. Jian, Y. Xu, X. Yang, W. Liu, M. Fu, H. Yu, F. Xu, F. Feng, L. Jia, D. Friedrich, R. van de Krol and H. Wang, *Nat. Commun.*, 2019, **10**, 2609.
105 M. Q. Pham, T. M. Ngo, V. H. Nguyen, L. X. Nong, D.-V. N. Vo, T. V. Tran, T.-D. Nguyen, X.-T. Bui and T. D. Nguyen, *Arabian J. Chem.*, 2020, **13**, 8388–8394.
106 X. Zhang, Z. Ai, F. Jia, L. Zhang, X. Fan and Z. Zou, *Mater. Chem. Phys.*, 2007, **103**, 162–167.
107 F. F. Abdi, S. P. Berglund and R. van de Krol, in *Photoelectrochemical Solar Fuel Production: From Basic Principles to Advanced Devices*, ed. S. Giménez and J. Bisquert, Springer International Publishing, Cham, 2016, pp. 355–391.
108 S. Tokunaga, H. Kato and A. Kudo, *Chem. Mater.*, 2001, **13**, 4624–4628.
109 N. D. Phu, L. H. Hoang, P. K. Vu, M.-H. Kong, X.-B. Chen, H. C. Wen and W. C. Chou, *J. Mater. Sci.: Mater. Electron.*, 2016, **27**, 6452–6456.
110 A. Kudo, K. Omori and H. Kato, *J. Am. Chem. Soc.*, 1999, **121**, 11459–11467.
111 B. Zhang, L. Wang, Y. Zhang, Y. Ding and Y. Bi, *Angew. Chem., Int. Ed.*, 2018, **57**, 2248–2252.
112 Q. Wang, T. Hisatomi, Y. Suzuki, Z. Pan, J. Seo, M. Katayama, T. Minegishi, H. Nishiyama, T. Takata, K. Seki, A. Kudo, T. Yamada and K. Domen, *J. Am. Chem. Soc.*, 2017, **139**, 1675–1683.
113 Q. Wang, T. Hisatomi, Q. Jia, H. Tokudome, M. Zhong, C. Wang, Z. Pan, T. Takata, M. Nakabayashi, N. Shibata, Y. Li, I. D. Sharp, A. Kudo, T. Yamada and K. Domen, *Nat. Mater.*, 2016, **15**, 611–615.
114 Q. Wang and K. Domen, *Chem. Rev.*, 2020, **120**, 919–985.
115 S. Liu, J. Pan, X. Li, X. Meng, H. Yuan, Y. Li, Y. Zhao, D. Wang, J. Ma, S. Zhu and L. Kong, *Nanoscale*, 2020, **12**, 14853–14862.
116 Z. Zhao, Z. Li and Z. Zou, *Phys. Chem. Chem. Phys.*, 2011, **13**, 4746–4753.
117 J. K. Cooper, S. Gul, F. M. Toma, L. Chen, P.-A. Glans, J. Guo, J. W. Ager, J. Yano and I. D. Sharp, *Chem. Mater.*, 2014, **26**, 5365–5373.
118 Y.-X. Ma, B. Gao, J. He, J.-F. Ma and Y. Zhao, *Chem. Eng. J.*, 2021, **422**, 130092.
119 H. Chen, S. Wang, J. Wu, X. Zhang, J. Zhang, M. Lyu, B. Luo, G. Qian and L. Wang, *J. Mater. Chem. A*, 2020, **8**, 13231–13240.
120 H. Tian, H. Wu, Y. Fang, R. Li and Y. Huang, *J. Hazard. Mater.*, 2020, **399**, 123159.
121 J. K. Cooper, S. Gul, F. M. Toma, L. Chen, Y.-S. Liu, J. Guo, J. W. Ager, J. Yano and I. D. Sharp, *J. Phys. Chem. C*, 2015, **119**, 2969–2974.
122 F. F. Abdi, T. J. Savenije, M. M. May, B. Dam and R. van de Krol, *J. Phys. Chem. Lett.*, 2013, **4**, 2752–2757.
123 M. Ziwritsch, S. Müller, H. Hempel, T. Unold, F. F. Abdi, R. van de Krol, D. Friedrich and R. Eichberger, *ACS Energy Lett.*, 2016, **1**, 888–894.
124 J. Yang, D. Wang, X. Zhou and C. Li, *Chem. – Eur. J.*, 2013, **19**, 1320–1326.
125 L. Chen, F. M. Toma, J. K. Cooper, A. Lyon, Y. Lin, I. D. Sharp and J. W. Ager, *ChemSusChem*, 2015, **8**, 1066–1071.

126 M. Li, L. Zhao and L. Guo, *Int. J. Hydrogen Energy*, 2010, **35**, 7127–7133.
127 M. Tayebi and B.-K. Lee, *Catal. Today*, 2021, **361**, 183–190.
128 W.-J. Yin, S.-H. Wei, M. M. Al-Jassim, J. Turner and Y. Yan, *Phys. Rev. B: Condens. Matter Mater. Phys.*, 2011, **83**, 155102.
129 V. Pasumarthi, T. Liu, M. Dupuis and C. Li, *J. Mater. Chem. A*, 2019, **7**, 3054–3065.
130 M. Xiao, Z. Wang, M. Lyu, B. Luo, S. Wang, G. Liu, H.-M. Cheng and L. Wang, *Adv. Mater.*, 2019, **31**, 1801369.
131 T. Das, X. Rocquefelte, R. Laskowski, L. Lajaunie, S. Jobic, P. Blaha and K. Schwarz, *Chem. Mater.*, 2017, **29**, 3380–3386.
132 M. Yabuta, A. Takeda, T. Sugimoto, K. Watanabe, A. Kudo and Y. Matsumoto, *J. Phys. Chem. C*, 2017, **121**, 22060–22066.
133 M. Lamers, S. Fiechter, D. Friedrich, F. F. Abdi and R. van de Krol, *J. Mater. Chem. A*, 2018, **6**, 18694–18700.
134 Z. Chen, Z. Liu, J. Zhan, Y. She, P. Zhang, W. Wei, C. Peng, W. Li and J. Tang, *Chem. Phys. Lett.*, 2021, **766**, 138342.
135 Z. Ma, H. Hou, K. Song, Z. Fang, L. Wang, F. Gao, W. Yang, B. Tang and Y. Kuang, *Chem. Eng. J.*, 2020, **379**, 122266.
136 L. Grad, Z. Novotny, M. Hengsberger and J. Osterwalder, *Sci. Rep.*, 2020, **10**, 10686.
137 S. Corby, L. Francàs, A. Kafizas and J. R. Durrant, *Chem. Sci.*, 2020, **11**, 2907–2914.
138 M. Kim, B. Lee, H. Ju, J. Y. Kim, J. Kim and S. W. Lee, *Adv. Mater.*, 2019, **31**, 1903316.
139 C. Zhu, C. Li, M. Zheng and J.-J. Delaunay, *ACS Appl. Mater. Interfaces*, 2015, **7**, 22355–22363.
140 Z. Wang and L. Wang, *EcoMat*, 2021, **3**, e12075.
141 G. Wang, Y. Yang, Y. Ling, H. Wang, X. Lu, Y.-C. Pu, J. Z. Zhang, Y. Tong and Y. Li, *J. Mater. Chem. A*, 2016, **4**, 2849–2855.
142 N. Österbacka and J. Wiktor, *J. Phys. Chem. C*, 2021, **125**, 1200–1207.
143 Y. Zhang, Y. Bu, F. Jiang, H. Li, X. Chen and J.-P. Ao, *Electrochim. Acta*, 2021, **366**, 137288.
144 Z. Wang, P. K. Nayak, J. A. Caraveo-Frescas and H. N. Alshareef, *Adv. Mater.*, 2016, **28**, 3831–3892.
145 M. D. Bhatt and J. Y. Lee, *J. Electroanal. Chem.*, 2018, **828**, 97–101.
146 F. A. Kröger and H. J. Vink, *J. Phys. Chem. Solids*, 1958, **5**, 208–223.
147 G. Wang, Y. Ling, X. Lu, F. Qian, Y. Tong, J. Z. Zhang, V. Lordi, C. R. Leao and Y. Li, *J. Phys. Chem. C*, 2013, **117**, 10957–10964.
148 Z. Tian, P. Zhang, P. Qin, D. Sun, S. Zhang, X. Guo, W. Zhao, D. Zhao and F. Huang, *Adv. Energy Mater.*, 2019, **9**, 1901287.
149 S. Jin, X. Ma, J. Pan, C. Zhu, S. E. Saji, J. Hu, X. Xu, L. Sun and Z. Yin, *Appl. Catal., B*, 2021, **281**, 119477.
150 Y. Zhang, X. Chen, F. Jiang, Y. Bu and J.-P. Ao, *ACS Sustainable Chem. Eng.*, 2020, **8**, 9184–9194.
151 H. L. Tan, A. Suyanto, A. T. D. Denko, W. H. Saputera, R. Amal, F. E. Osterloh and Y. H. Ng, *Part. Part. Syst. Charact.*, 2017, **34**, 1600290.
152 J. Li, L. Guo, N. Lei, Q. Song and Z. Liang, *ChemElectroChem*, 2017, **4**, 2852–2861.
153 Y. Peng, H. Wu, M. Yuan, F.-F. Li, X. Zou, Y. H. Ng and H.-Y. Hsu, *Sustainable Energy Fuels*, 2021, **5**, 2284–2293.
154 D. Xu, Y. Liu, Y. Zhang, Z. Shi, M. Yang, C. Zhang and B. Liu, *Chem. Eng. J.*, 2020, **393**, 124693.
155 Y. Bu, J. Tian, Z. Chen, Q. Zhang, W. Li, F. Tian and J.-P. Ao, *Adv. Mater. Interfaces*, 2017, **4**, 1601235.
156 X. Yin, J. Li, L. Du, F. Zhan, K. Kawashima, W. Li, W. Qiu, Y. Liu, X. Yang, K. Wang, Y. Ning and C. B. Mullins, *ACS Appl. Energy Mater.*, 2020, **3**, 4403–4410.
157 X. Chen, D. Wang, Y. Huang, Y. Zhang, C. Li, S. Wang, Y. Liu and X. Zhang, *APL Mater.*, 2020, **8**, 031112.
158 Q. Qin, Q. Cai, J. Li, C. Jian, W. Hong and W. Liu, *Sol. RRL*, 2019, **3**, 1900301.
159 Q. Pan, K. Yang, G. Wang, D. Li, J. Sun, B. Yang, Z. Zou, W. Hu, K. Wen and H. Yang, *Chem. Eng. J.*, 2019, **372**, 399–407.
160 M. Fang, Q. Cai, Q. Qin, W. Hong and W. Liu, *Chem. Eng. J.*, 2021, **421**, 127796.
161 Y. Luo, G. Tan, G. Dong, H. Ren and A. Xia, *Appl. Surf. Sci.*, 2016, **364**, 156–165.
162 Y. Zhang, X. Zhang, D. Wang, F. Wan and Y. Liu, *Appl. Surf. Sci.*, 2017, **403**, 389–395.
163 X. Yang, A. J. Fernández-Carrión, J. Wang, F. Porcher, F. Fayon, M. Allix and X. Kuang, *Nat. Commun.*, 2018, **9**, 4484.
164 B. Anke, M. Rohloff, M. G. Willinger, W. Hetaba, A. Fischer and M. Lerch, *Solid State Sci.*, 2017, **63**, 1–8.
165 F. S. Hegner, D. Forrer, J. R. Galán-Mascarós, N. López and A. Selloni, *J. Phys. Chem. Lett.*, 2019, **10**, 6672–6678.
166 Y. Yuan, Y. Huang, F. Ma, Z. Zhang and X. Wei, *J. Mater. Sci.*, 2017, **52**, 8546–8555.
167 G. Liu, H. G. Yang, J. Pan, Y. Q. Yang, G. Q. Lu and H.-M. Cheng, *Chem. Rev.*, 2014, **114**, 9559–9612.
168 X. Chen, L. Liu, P. Y. Yu and S. S. Mao, *Science*, 2011, **331**, 746–750.
169 J. Gan, X. Lu, B. B. Rajeeva, R. Menz, Y. Tong and Y. Zheng, *ChemElectroChem*, 2015, **2**, 1385–1395.
170 H. Seo, Y. Ping and G. Galli, *Chem. Mater.*, 2018, **30**, 7793–7802.
171 X. Gu, Y. Luo, Q. Li, R. Wang, S. Fu, X. Lv, Q. He, Y. Zhang, Q. Yan, X. Xu, F. Ji and Y. Qiu, *Front. Chem.*, 2020, **8**, 601983.
172 Y. Zhang, J. Bai, J. Wang, S. Chen, H. Zhu, J. Li, L. Li, T. Zhou and B. Zhou, *Chem. Eng. J.*, 2020, **401**, 126134.
173 S. Selim, E. Pastor, M. Garcia-Tecedor, M. R. Morris, L. Francas, M. Sachs, B. Moss, S. Corby, C. A. Mesa, S. Gimenez, A. Kafizas, A. A. Bakulin and J. R. Durrant, *J. Am. Chem. Soc.*, 2019, **141**, 18791–18798.
174 S. Wang, T. He, J.-H. Yun, Y. Hu, M. Xiao, A. Du and L. Wang, *Adv. Funct. Mater.*, 2018, **28**, 1802685.

175 W. Wang, P. J. Strohbeen, D. Lee, C. Zhou, J. K. Kawasaki, K.-S. Choi, M. Liu and G. Galli, *Chem. Mater.*, 2020, **32**, 2899–2909.
176 Y. Zhang, Y. Guo, H. Duan, H. Li, C. Sun and H. Liu, *Phys. Chem. Chem. Phys.*, 2014, **16**, 24519–24526.
177 J. Hu, X. Zhao, W. Chen, H. Su and Z. Chen, *J. Phys. Chem. C*, 2017, **121**, 18702–18709.
178 X. Zhao, J. Hu, X. Yao, S. Chen and Z. Chen, *ACS Appl. Energy Mater.*, 2018, **1**, 3410–3419.
179 J.-M. Wu, Y. Chen, L. Pan, P. Wang, Y. Cui, D. Kong, L. Wang, X. Zhang and J.-J. Zou, *Appl. Catal., B*, 2018, **221**, 187–195.
180 A. Kahraman, M. B. Vishlaghi, I. Baylam, H. Ogasawara, A. Sennaroğlu and S. Kaya, *J. Phys. Chem. Lett.*, 2020, **11**, 8758–8764.
181 Y. Pihosh, I. Turkevych, K. Mawatari, J. Uemura, Y. Kazoe, S. Kosar, K. Makita, T. Sugaya, T. Matsui, D. Fujita, M. Tosa, M. Kondo and T. Kitamori, *Sci. Rep.*, 2015, **5**, 11141.
182 C. Cheng, Q. Fang, S. Fernandez-Alberti and R. Long, *J. Phys. Chem. Lett.*, 2021, **12**, 3514–3521.
183 L. Pan, J. H. Kim, M. T. Mayer, M.-K. Son, A. Ummadisingu, J. S. Lee, A. Hagfeldt, J. Luo and M. Grätzel, *Nat. Catal.*, 2018, **1**, 412–420.
184 D. Huang, K. Wang, L. Li, K. Feng, N. An, S. Ikeda, Y. Kuang, Y. Ng and F. Jiang, *Energy Environ. Sci.*, 2021, **14**, 1480–1489.
185 S. Ye, W. Shi, Y. Liu, D. Li, H. Yin, H. Chi, Y. Luo, N. Ta, F. Fan, X. Wang and C. Li, *J. Am. Chem. Soc.*, 2021, **143**, 12499–12508.